IV WISE field experiments data processing and results. Inter-comparison with theoretical models

IV.1 Introduction

In this chapter, an explanation of the WISE radiometric measurements and surface foam coverage data processing is given. First, the WISE results related to the T_B dependence with the wind speed, the incident and azimuth position are presented and compared to theoretical models. The following sections are devoted to establish the relationship between the sea foam coverage and the sea state with the brightness temperature as well as to present the statistical results from the WISE experiment concerning to the foam and the whitecap phenomenology. A first inter-comparison between the WISE results and a two-layer theoretical foam model [24] and [25] is made in this section. Further analysis is provided in the study of FROG data (Chapter VI).

IV.2 Data processing

IV.2.1 Raw data input files and data pre-processing

Raw radiometric data, meteorological and surface foam coverage images from the Ultrak KC550xCP video camera were simultaneously acquired using the industrial PC to save. Additional sea surface temperature, wind speed and direction information from the oceanographic buoys, the infrared thermal radiometer, and oil rig meteorological station data were acquired. Finally, the sea surface salinity data from water samples were analyzed.

First, the different data had to be formatted because the radiometric and the UPC meteorological data were collected at a rate of one second, while meteorological data from oil rig station was taken every 15 minutes, and from the meteorological buoy (Buoy 2, chapter III) every 2 minutes.

During WISE 2000 field experiment the radiometric data was continuously stored using the naming and structure described in the following paragraphs. For each new date, a directory named `yymmdd` is created, which contains all the files generated in this date. At the end of every day, all files included in this directory were copied to a CD-Rom as a backup and for later processing. The schematic file structure was:

[rootdir]

`yymmdd`	(data directory)
`raw`	(raw data directory)
`yymmdd.dck`	(Dicke calibration data file)
`yymmdd.pol`	(correlator calibration data file)
`yymmdd[NN].raw`	(radiometric data file)

`yymmdd[NN].met` (meteorological data file)

There were four different types of files:

- The Dicke calibration data files (one per day): included the calibration starting date and time, the data related to the calibrations (cold and hot voltages sources) of the two receivers (horizontal and vertical polarization), and the "*a*" (voltage sensitivity) and "*b*" (offset sensitivity) parameters of the line fit of the output voltages of the receivers and the T_A. Each Dicke calibration (4 minutes) was saved in one line (ASCII).
- The correlator calibration data file (one per day): used to save the calibration starting date and time, and the data related to the complex digital correlator. Each correlator calibration was saved in one line (ASCII).
- The radiometric data files, `yymmdd[NN].raw` (from the LAURA radiometer) where the [NN] stands for a two-digit sequential number starting at 00 each day. All data files are ASCII files, and they contain a indefinite number of lines, each one corresponding to a single measurement, and the following fields in each line:
  - Julian day (number of days within the year),
  - GPS UTC time (hours, minutes and seconds) at 1 s interval,
  - Vertical and horizontal receivers detector output voltages (V_H, V_V),
  - Digital correlator counts (N_{i_V,i_H}, N_{q_V,i_H}, N_{total}) needed to compute 3rd and 4th Stokes parameters,
  - Output voltages of internal temperature sensors (T_{refH}, T_{refV}, T_{int}, T_{ph_corr}),
  - Radiometer position: (incidence and azimuth position), and
  - Clinometer's pitch, yaw and roll.
- The meteorological data file (from UPC meteorological station), where the [NN] stands for a two-digit sequential number starting at 00 each day. All data files are of ASCII files, and they contain a indefinite number of lines, each one corresponding to a single measurement, and the following fields in each line:
  - Julian day (number of days within the year),
  - GPS UTC time (hours, minutes and seconds) at 1 s interval,
  - Temperature from UPC meteorological sensors: control unit (CU), T_{ph_abs} (hot load sensor), T_{ms_ext} (environment) T_{ms_int} (LAURA radiometer),
  - Relative humidity inside (RHi_{nt}) and outside (RH_{ext},) of the LAURA radiometer,

- ♦ Wind speed and wind direction (WS, WD),
- ♦ Rain counts, and
- ♦ Pressure.

During WISE 2001, the files structure was reduced to a single file that included all the information of the Dicke and the complex correlation calibration files, the radiometric and meteorological data to simplify the data formatting process. To do this, a new parameter called operation mode (calibration or measurement) was included in the input files. A brief description of the fields for all data files is given in the following paragraphs.

Radiometric data files: these files contain the radiometer's output, the digital clinometer (during WISE 2000), analog clinometer (during WISE 2001), pitch information, the meteorological data, as well as information about the radiometer physical temperature. In order to avoid huge files, several ones are created automatically, being [NN] the sequential number. A new file can be created for several reasons: 1) maximum size is limited to 5,000 lines (~900 Kbytes), 2) start a new sequence, or 3) the sequence process has been aborted. The fields are divided in the next parameters:

- Julian day (number of days within the year),
- GPS UTC time (hours, minutes and seconds) at 1 s interval,
- Operation mode[2]: measurements (0), hot load calibration (1), cold load calibration (2).
- Radiometer position: (incidence and azimuth position),
- Clinometer's pitch,
- Vertical and horizontal receivers detector output voltages (V_H, V_V),
- Digital correlator counts ($N_{i_v,i_h}, N_{q_v,i_h}, N_{total}$) needed to compute 3rd and 4th Stokes parameters,
- Output voltages of internal temperature sensors (T_{refH}, T_{refV}, T_{int}, T_{ph_corr}),
- Output voltages of external (environment) temperature sensors (T_{ext}),
- Temperature from UPC meteorological sensors: control unit (CU), T_{ph_abs} (hot load sensor), T_{ms_ext} (environment), T_{ms_int} (LAURA radiometer),
- Relative humidity inside (RHi_{nt}) and outside (RH_{ext},) of the LAURA radiometer,
- Wind speed and wind direction (WS, WD),
- Rain counts, and

[2] The operation mode for the uncorrelated and correlated loads is 0, when the antenna is pointing to the sky.

- Pressure.

The raw data pre-processing consisted of the following steps:

- All the sequences were separated sequentially and according to the four types of measurements. In other words, every sequence is composed by a calibration at the beginning and at the end of the sequence, and an incidence, or azimuth scan, or a fixed position measurement. Files are saved as Matlab files and printed to be analyzed.
- Unfortunately during WISE 2000 an important number of samples were corrupted by RFI (Chapter III). One of the previous tasks prior to the calibration of T_B consisted of eliminating the corrupted samples manually.
- Finally, radiometric, oceanographic buoys and oil rig meteorological data were all formatted at a common rate of 1 sample per second.

Files were saved into a Matlab matrix. The schematic structure is the following:

```
[rootdir]
    [α]                                  (data level 1)
        yymmdd                           (data level 2)
            mat                          (mat data directory)
                [α]yymmdd[NN].mat        (data file)
```

where [α] is replaced by A,B,C,... according to the pre-processing levels, (separation of the sequences, RFI elimination, radiometric, oceanographic buoys and meteorological assembly of data), and [NN] corresponds to the complete sequence (incidence, azimuth or fixed measurement, including the calibrations).

IV.2.2 Radiometric data processing

The pre-processed raw data files were processed to obtain the final Stokes parameters. The final data structure is the same as in the pre-processing data files. As some corrections are necessary before the Stokes vector is obtained, different [α] files are generated.

The brightness temperatures (T_H and T_V) of the scene are obtained by computing the "*a*" and "*b*" parameters from the cold and hot measurements from which the measured antenna temperature are obtained:

$$V_{B_{H,V}} = a \cdot \left(T_{A_{H,V}}^{measured} - T_{ref} \right) - b, \tag{4.1}$$

where:

- $V_{B_{H,V}}$ is the measured voltage at the output of the radiometer,

- $T_{A_{H,V}}^{measured}$ its corresponding antenna temperature, and
- T_{ref} the reference load temperature,

The corrected brightness temperature is derived from $T_{A_{H,V}}^{measured}$ to account for the scattered radiation and the antenna finite beamwidth effects.

$$T_{B_{H,V}}^{c} \cong T_{A_{H,V}}^{measured} - (1 - e_w) \cdot T_{DN} + \Delta T_{A_{H,V}}^{finite\ beam} \quad , \tag{4.2}$$

where:

e_w is the emissivity of the sea water,

T_{DN} is the atmospheric downward emission and,

$\Delta T_{A_{H,V}}^{finite\ beam}$ is the correction due to the finite beamwidth effects.

The contribution of the sky (T_{DN}) was computed from the Liebe atmospheric model plus the cosmic background (2.7 K) and galactic noise maps at 1420 MHz weighted by the antenna pattern for all the sequences. These values depend on the incidence angle, geographic location, time and data and were subtracted from the measured brightness T_B. The scattered brightness temperatures depend also on the following parameters: the sea surface temperature and salinity, the wind speed, the atmospheric pressure, the atmospheric temperature and humidity. To minimize the computational cost, the algorithm is applied once per angle position.

The second contribution to be corrected is due to the LAURA's antenna beamwidth effects ($\Delta\theta_{-3dB} \sim 20°$). The spatial averaging causes that the measured Stokes parameters be a linear combination of the true ones. Simulation results over calm salt water for LAURA's antenna pattern (including secondary lobes) show a bias between the antenna temperature and the brightness temperature (Figure 4.1), which depends on the incidence angle.

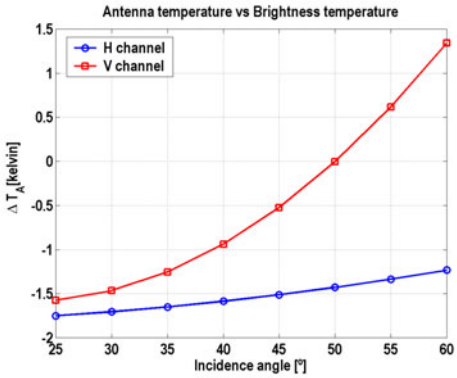

Figure 4.1. Bias between the antenna temperature and the brightness temperature at the nominal incidence angle, for LAURA's antenna due to finite beamwidths effects.

The processed files with the calibrated instantaneous brightness temperatures were then screened to eliminate samples that deviate more than 3σ from the mean value, as they are suspected to suffer from RFI.

The atmospheric stability correction [26] was applied to the wind speed data to account for the air-sea temperature difference. A set of new data files were generated and the brightness temperature samples were averaged every 5 minutes to increase the radiometric sensitivity (reduce noise).

The final data (ASCII files) was presented separating the type of scan (incidence, azimuth or fixed position) and sequences, separated by days. The following final WISE data were presented:

- Julian day (number of days within the year),
- The starting and ending UTC time of that particular sequence,
- The radiometer's incidence and azimuth position [°],
- The four Stokes parameters in Kelvin, (only T_H and T_V in WISE 2001 due to a correlator failure) and their corresponding deviations
- The downwelling temperature in Kelvin computed according to the model,
- The measured physical temperature of the microwave absorber (hot load source), and
- The rain rate in [mm/h] collected by the UPC rain gauge.

IV.2.3 Foam data processing

Video imagery was acquired simultaneously with the video camera pointing to the same FOV than the radiometer. Video sequences were saved into the hard disk in a (avi format, lossless compression codec). The file structure was the following:

[rootdir]

`yymmdd` (data directory)

`[type][NN].avi` (file name)

For each new date, a directory named `yymmdd` was created containing all the files generated in this date. The file name chosen depends on the type of sequence (incidence, azimuth scan or fixed position) and the sequence number.

The video processing consisted of separating each photogram and masking them to match the antenna beamwidth (Figure 4.2a). Since each image pixel corresponds to a different distance and incidence angle, its area was first determined.

(a) 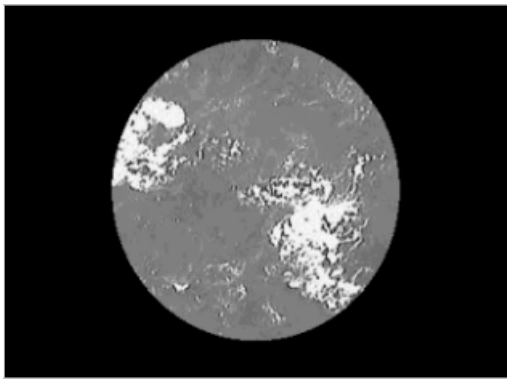 (b) 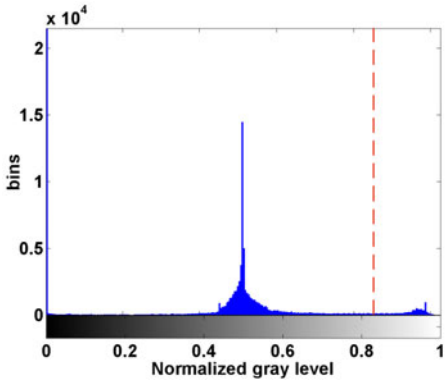

Figure 4.2. (a) Sample photogram masked to match the radiometer's beamwidth, and (b) its histogram. The dotted line shows the threshold. Pixels above the threshold are foam-covered.

The determination of foam-covered pixels consisted of computing the image histogram and selecting the pixels with grey levels higher than a given threshold. The threshold was found for each illumination condition as the grey level corresponding to minimum between the two peaks in the bi-modal distribution (Figure 4.2b). Foam data including the UTC time and the foam percentage were saved into a ASCII file in its corresponding directory `yymmdd`. The foam percentage column is then added to the radiometric data file to simplify the data processing.

IV.3 WISE results: Sea state effects on the instantaneous brightness temperature (T_B)

IV.3.1 Incidence scan measurements: Inter-comparison with the theoretical models

IV.3.1.1 Brightness temperature sensitivity to wind speed derived from the WISE measurements

One of the main goals of the WISE field experiment was the determination of the wind speed contribution to the brightness temperature, since this effect can mask the signature due to the salinity. On the other hand, these measurements are necessary to improve the best parameterization of the numerical models.

The wind-induced brightness temperature $\Delta T_{B_{h,v}}(\theta, U_{10})$ is derived from the flat surface emissivity model (eqns. (4.3) to (4.5)) as:

$$T_{B_{H,V}}(\theta, SST, SSS, U_{10}) = T_{B_{H,V}}^{Fresnel}(\theta, SST, SSS) + \Delta T_{B_{H,V}}(\theta, U_{10}) \,, \tag{4.3}$$

where

$$T_{B_{H,V}}^{Fresnel}(\theta, SST, SSS) = SST \cdot e_{H,V}(\theta, SST, SSS) \,, \tag{4.4}$$

is the brightness temperature of the flat sea surface, and

$$e_{H,V}(\theta, SST, SSS) = 1 - \left|\Gamma_{H,V}(\theta, SST, SSS)\right|^2 . \quad (4.5)$$

is the emissivity computed from the Fresnel field reflection coefficient at H- and V-polarizations using the Klein and Swift dielectric permittivity model [27].

Figure 4.3 presents typical measurements of incidence scans, at horizontal (left) and vertical polarizations (right) for two different wind speeds: 1.3 m/s (a-b) and 11.9 m/s (c-d), (WISE 2000). The wind speeds correspond to U_{10} averaged during the measurement interval. During WISE 2000, the trend is almost always the theoretical one: a brightness temperature increase at H-polarization with increasing wind speed and decreasing incidence angle, and increasing at V-polarization with increasing wind speed and incidence angle incidence angles, below ~55°, but decreasing with increasing wind speed above ~55°. Figure 4.3 shows some exceptions: an increase at higher incidence angles (65º, and sometimes 55º) at horizontal polarization, and a decrease at low incidence angle (25º) at vertical polarization. The increase at horizontal polarization was clearly identified as radio frequency interference (RFI) coming from the coast of Tarragona, and was minimized/avoided by taking most of the measurements to the West. The decrease at vertical polarization seemed to be due to the metallic structure of the Casablanca oil rig.

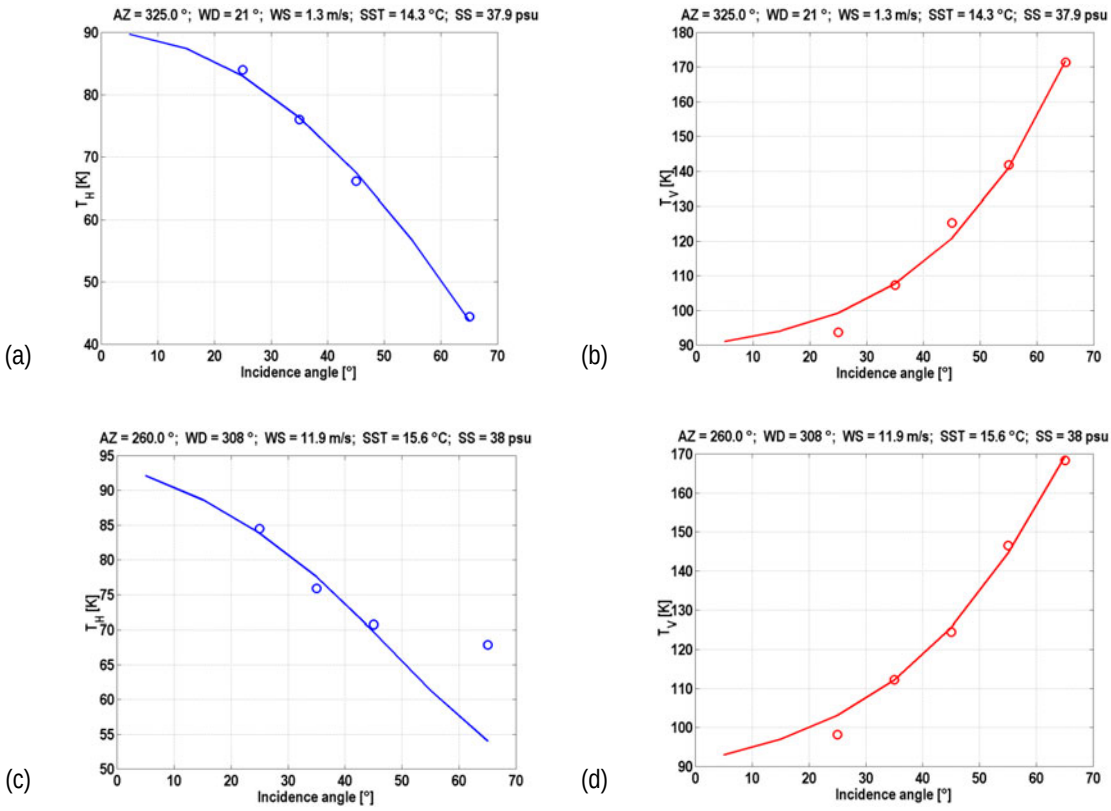

Figure 4.3. Sample measurements of incidence angle scans at horizontal (left) and vertical polarizations (right) for wind speeds: 1.3 m/s (a-b) and 11.9 m/s (c-d) corresponding to WISE 2000.

Numerical models predict a quasi-linear dependence between the wind speed and the brightness temperature for moderate wind speeds (lower than 10-12 m/s). At higher wind speeds, the foam effect (as it can be seen later) must be considered. During WISE 2000 the wind conditions were low moderate, and

the atmosphere was stable most of the time. To determine the relationship between the Stokes parameters and the wind speed, the corresponding data points were sorted by polarization and incidence angle.

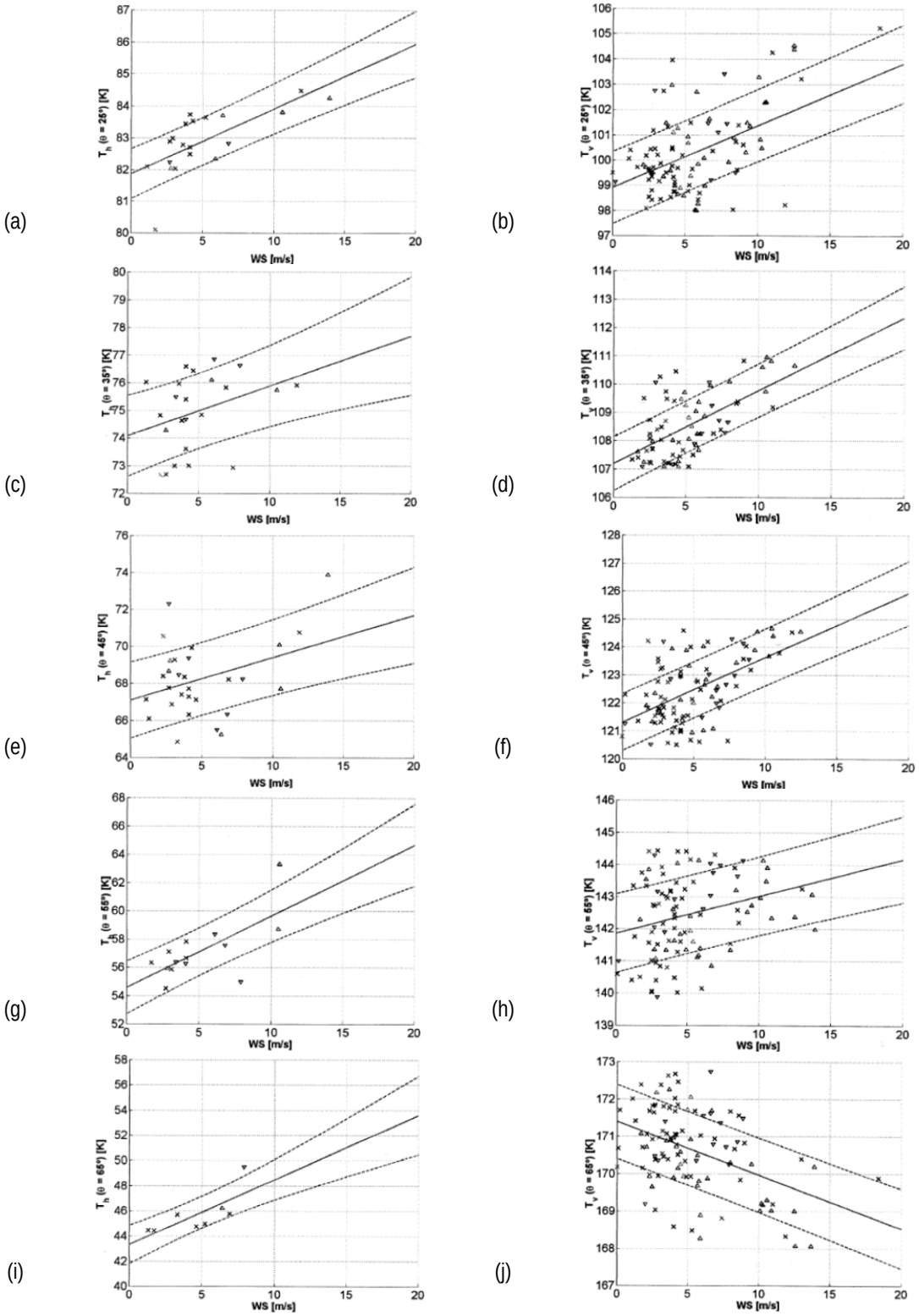

Figure 4.4. Brightness temperature dependence vs. U_{10} at H- and V- polarizations at different incidence angles: (a) and (b) 25°, (c) and (d) 35°, (e) and (f) 45°, (g) and (h) 55°, and (i) and (j) 65°. Wind direction relative to the radiometer: Δ = up-wind, ∇ = down-wind, x = cross-wind

Then, anomalous data was eliminated those exceeding the $\pm 3\sigma$ from the linear regression were suspected to be wrong or corrupted by RFI and were filtered out. Figure 4.4a to j show the L-band brightness temperature at horizontal (left) and vertical (right) polarizations at different incidence angles, (25° to 65° in steps of 10°) plotted respect to U_{10}.

Unfortunately, due to the high RFI encountered during WISE 2000, the number of remaining data points was not large (Table 4.1), and the associated error bars were large. As it can be appreciated, the number of data points is much smaller at horizontal polarization because of the larger RFI, and decreases dramatically at higher incidence angles. This induces larger uncertainties in the estimation of the wind speed sensitivity. Part of the error bars seemed to be due to the uncertainty in the wind speed estimation, its natural variability, and the errors in computing U_{10} from the oil rig meteorological station ($U_{69\,m}$), and U_{10} from the meteorological buoy ($U_{2.6\,m}$) [29], ($\sigma_{U_{10}(oil\,rig\,meteo)-U_{10}(buoy\,meteo)} \approx 1.8$ m/s).

Table 4.1. Number of data points for each incidence angle and polarization in WISE 2000.

θ	25°	35°	45°	55°	65°
H-polarization	20	23	29	14	8
V-polarization	100	74	98	102	100

Results are shown in Figure 4.5, and are in reasonable agreement with Hollinger [28] and Swift [30] measurements, with reduced error bars and give an extrapolated sensitivity at nadir of ~0.22 K/(m/s).

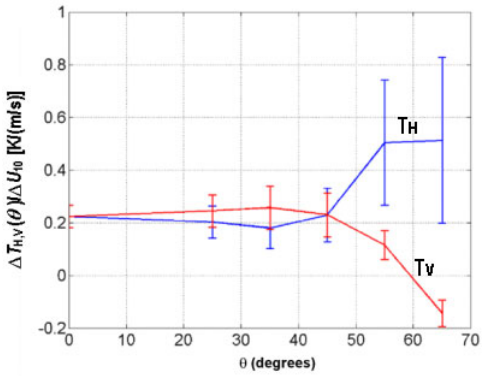

Figure 4.5. Sensitivity of T_H and T_V to wind speed at 10 m height and associated error bars

The sensitivity to U_{10} was found to increase at horizontal polarization, and to decrease at vertical polarization, and around $\theta \sim 60°$ the brightness temperature at vertical polarization becomes insensitive to wind speed. However, the fact that, at low incidence angles, the sensitivity of T_V to wind speed is larger than that of T_H -although within the error bars- is a behavior that is neither predicted by models, nor present in Hollinger's [28] measurements. Probably this phenomenon was due to the presence of swell and /or by the reflections on the oil rig structure.

During WISE 2001, the meteorological and oceanographic conditions were the most extreme ones registered on the oil rig during the last 20 years. Figure 4.6 shows a summary of the main oceanographic and meteorological parameters. During more than one third of the campaign wind speed well exceed 10

m/s, reaching more than 25 m/s, when the strongest storm happened. Peak waves were larger than 12 m and destroyed the 7 m deck of the oil rig. In this storm, the memory of Buoy 1 and the ultrasonic anemometer of Buoy 2 were also destroyed, and from this date to the end of the campaign wind data from the meteorological station of the oil rig had to be used. The measured sea surface salinity was very stable during the whole campaign, around 38 psu, except on November 18th due to an intense rain event. The sea surface temperature showed the start of the cooling from the warm summer value 22°C down to 16°C. At the beginning of the campaign, the atmosphere was stable, but quickly changed to unstable conditions (T_{sea}-T_{air} ≈ -6°C to -12°C). Since wind speed measurements have to be referred from 2.6 m and 70 m (U_{70} only wind data after November 15th, 2001) to 10 m height (U_{10}), and the atmospheric conditions were quite unstable, atmospheric instability corrections were applied [26].

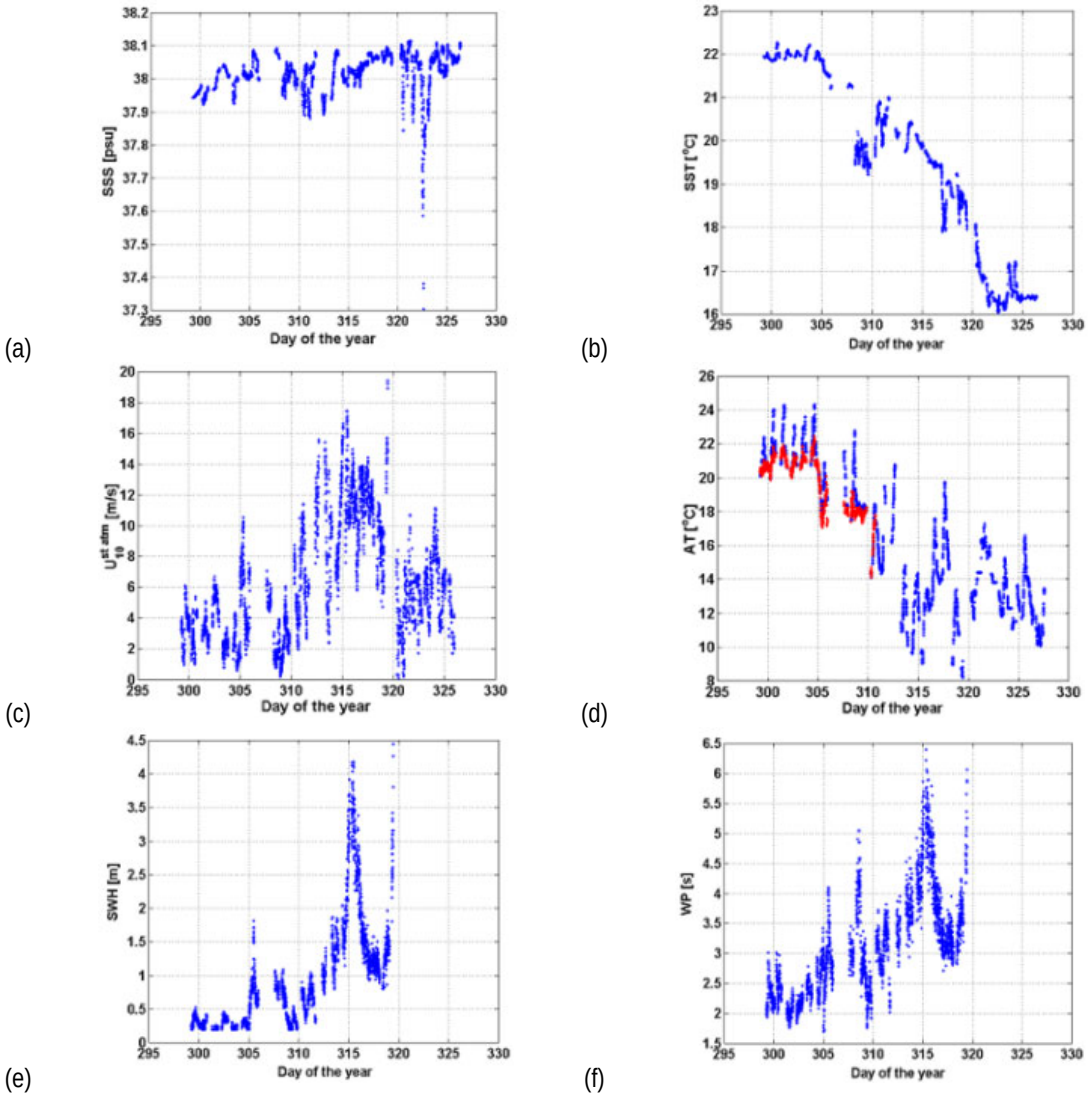

Figure 4.6. Main oceanographic and meteorological parameters during WISE 2001: (a) Sea surface salinity, (b) sea surface temperature, (c) wind speed referred to 10 m height, (d) atmospheric temperature, (e) significant wave height, and (f) wave period. Until day 305 atmospheric conditions were stable, but after it the sea was significantly warmer than the air (unstable atmosphere).

Figure 4.7 presents typical measurements of incidence scans, at horizontal (left) and vertical polarizations (right) for two different wind speeds: 0.6 m/s (a-b) and 13 m/s (c-d), (WISE 2001). As in

WISE 2000 field experiment, the brightness temperature increase at H-polarization with increasing wind speed and incidence angle, and increasing at V-polarization with increasing wind speed and incidence angle for small, below ~45. On the other hand, at high incidence angles (above ~45°) the increase at horizontal polarization and decrease at vertical polarization confirms the trend of the wind-induced ΔT_B from WISE 2000 results.

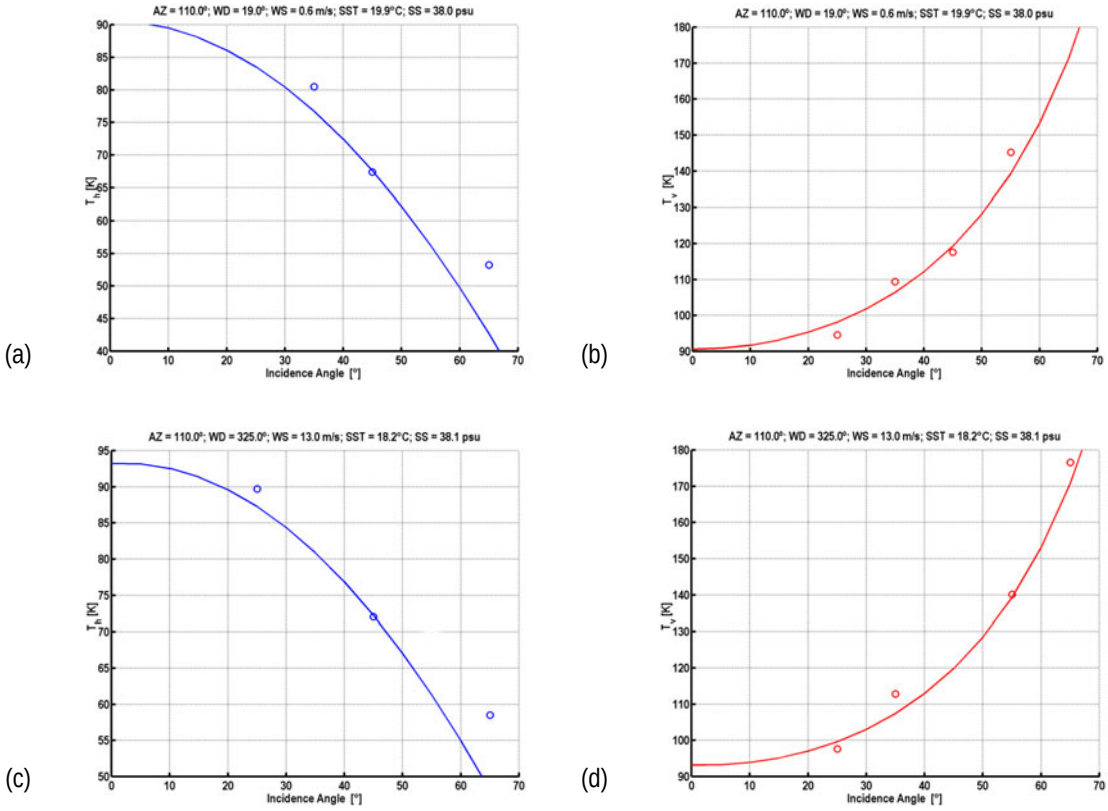

Figure 4.7. Sample measurements of incidence angle scans at horizontal (left) and vertical polarizations (right) for wind speeds: 0.6 m/s (a-b) and 13 m/s (c-d) corresponding to WISE 2001.

The derivation of the brightness temperature sensitivity to wind speed follows the same steps, but the number of data points is much larger (Table 4.2), since incidence angles at 30°, 40°, 50° and 60°, corresponding to the afternoon-evening measurements pointing to the North East, are also available.

Wind-induced WISE 2001 results are presented in Figure 4.8. It shows the plots of the brightness temperatures deviation due to wind ($\Delta T_{h,v}(U_{10})$), at horizontal (upper row) and vertical (center row) polarizations versus the wind speed at 10 m (U_{10}), for incidence angles from 25° to 65°, in 5° steps. The solid line in each plot represents the regression line and the dashed ones the ±50% percentile ones. Each point is the result of averaging the instantaneous measurements (τ = 1 s) during 5 minutes. Note that $\Delta T_{h,v}(U_{10})$ exhibits a positive bias at 30°, 35° and 60°, and a negative bias at 45° and 50°. The plot at the lower part of Figure 4.8 shows the slope of each regression line as a function of the incidence angle, which corresponds to the average sensitivity to wind speed in K/(m/s) at H- and V-polarizations. A linear fit of these values leads to the following relationships eqns. (4.6) and (4.7):

$$\Delta T_H(U_{10}) = 0.23 \cdot \left(1 + \theta/70^\circ\right) \cdot U_{10} \ , \tag{4.6}$$

$$\Delta T_V(U_{10}) = 0.23 \cdot \left(1 - \theta/50^\circ\right) \cdot U_{10} \ . \tag{4.7}$$

that leads an extrapolated sensitivity at nadir of:

$$\Delta T_{H,V}(U_{10}, \theta = 0°)/\Delta U_{10} = 0.23 K/(m/s) \tag{4.8}$$

Table 4.2. Number of data points for each incidence angle and polarization in WISE 2000.

θ	25°	30°	35°	40°	45°	50°	55°	60°	65°
H-polarization	143	36	232	35	478	33	348	36	125
V-polarization	305	34	532	56	656	57	511	49	190

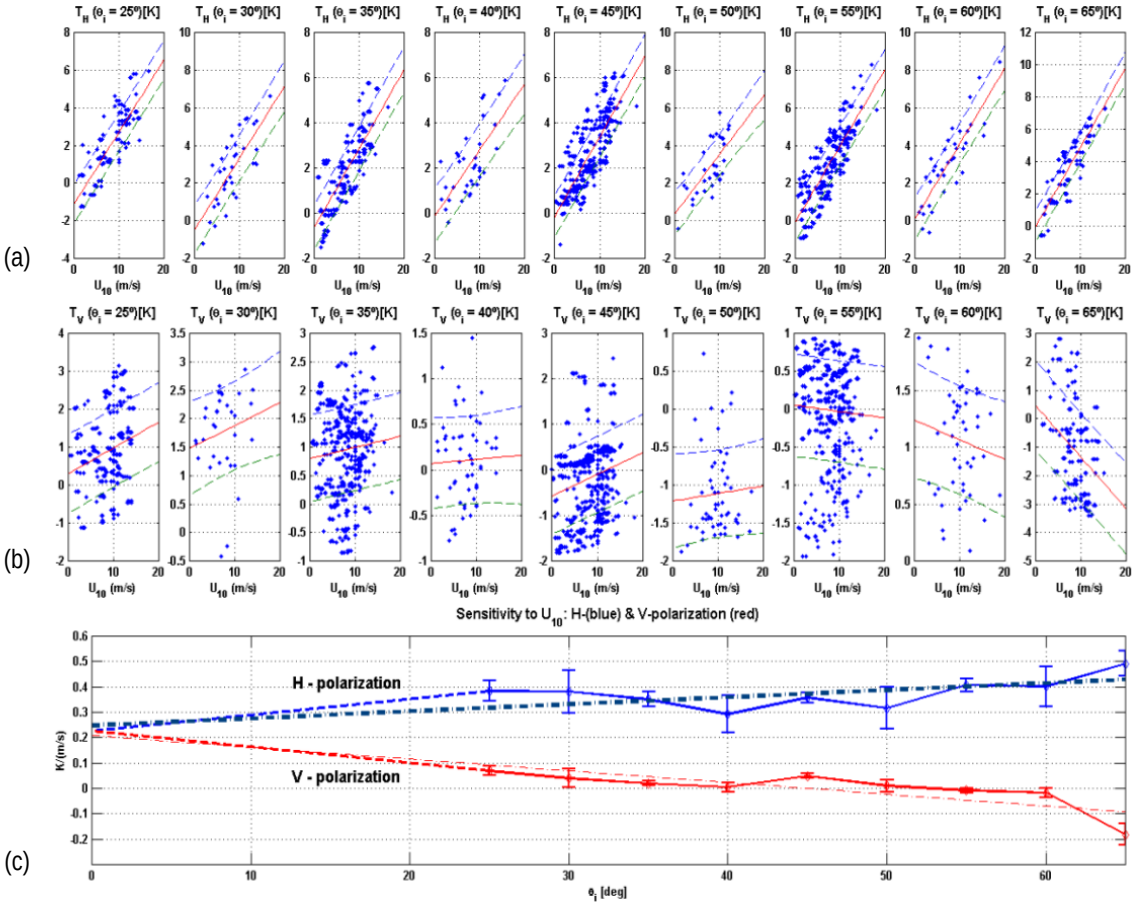

Figure 4.8. Derivation of the brightness temperature sensitivity to wind speed: (a) $\Delta T_H(U_{10})$ and (b) $\Delta T_V(U_{10})$ scatter plots, linear fit (solid line) and percentile 50% (dashed lines) as a function of wind speed for incidence angles from 25° to 65°. (c) Derived wind speed (U_{10}) sensitivity as a function of polarization and incidence angle. All data points used.

If [26] is used to try to correct for atmospheric instability when estimating the 10 m wind speed from 70 or 2.6 m height wind speed measurements, the resulting brightness temperature sensitivity to wind speed at nadir is slightly higher, (eqn. (4.9)):

$$\Delta T_{H,V}\left(U_{10},\theta=0°\right)/\Delta U_{10}=0.25K/\left(m/s\right) \tag{4.9}$$

IV.3.1.2 Inter-comparison between WISE measurements and the theoretical models

WISE 2000 data were compared with the two scale model [31] (formerly used to validate radiometric data, Ka-band). This model (Figure 4.9a) has implemented by Dinnat using three different wave spectra (Durden and Vesecky, Elfouhaily, and Durden and Vesecky multiplied by two). The WISE 2000 wind-induced brightness temperature versus the incidence angle at the H- and V-polarization are presented in Figure 4.9 b. WISE 2000 data are compared with the Hollinger measurements and the Yueh-LODYC using the Durden and Vesecky wave spectrum multiplied by two. It can be appreciated, WISE 2000-derived sensitivities are in agreement with the third LODYC model, although some parameters as foam, swell and others, have not included in the model.

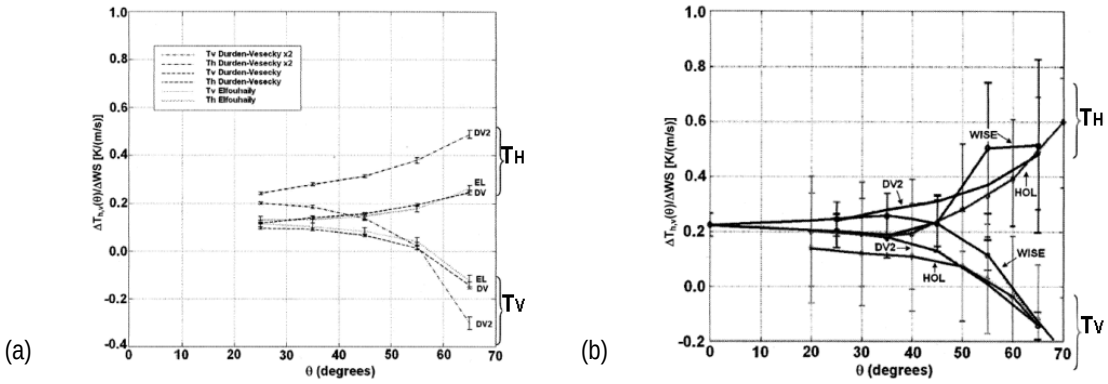

Figure 4.9. (a) Sensitivity of $T_{H,V}$ to U_{10} derived from Yueh-LODYC model with three different spectra and, (b) WISE 2000-derived brightness temperature sensitivities to U_{10} at H- and V- polarizations, comparison with the Hollinger's measurements and the Yueh-LODYC two-scale model (Durden and Vesecky spectrum x2).

From the analysis of the different numerical models referred to the sea surface roughness characterizations and the sea foam emission and coverage [32] the brightness temperature sensitivity to wind speed was computed with the SSA (small slope approximation) method, for three different sea surface spectra: Elfouhaily [33], Durden and Vesecky [34] and Elfouhaily et al. [33] (these two last wave spectra multiplied by 2 [32]). Figure 4.11 shows the brightness temperature sensitivity to wind speed as a function of wind speed and incidence angle computed with SSA method and the Elfouhaily and Durden and Vesecky spectra (both multiplied by 2). From the inspection of these figures, the following considerations can be appreciated:

- At low incidence angles the predicted dependence is well estimated for the two spectra,
- The $\Delta T_H/\Delta U_{10}$ is overestimated for high incidence angles (50-55°),

The behavior of $\Delta T_V/\Delta U_{10}$ does not obtain neither a null value around 55°, nor negative values at higher incidence angles.

From the inspection of the inter-comparison between the results and the wind-induced brightness temperature measurements from WISE 2001 (Figure 4.8), weighted by the U_{10} histogram from WISE field experiments (Figure 4.10), it can observed that SSA model underestimates the dependence for small incidence angles if Elfouhaily spectrum is applied.

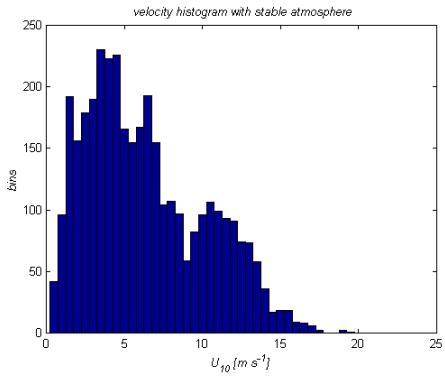

Figure 4.10. U10 histogram from WISE 2001 field experiment

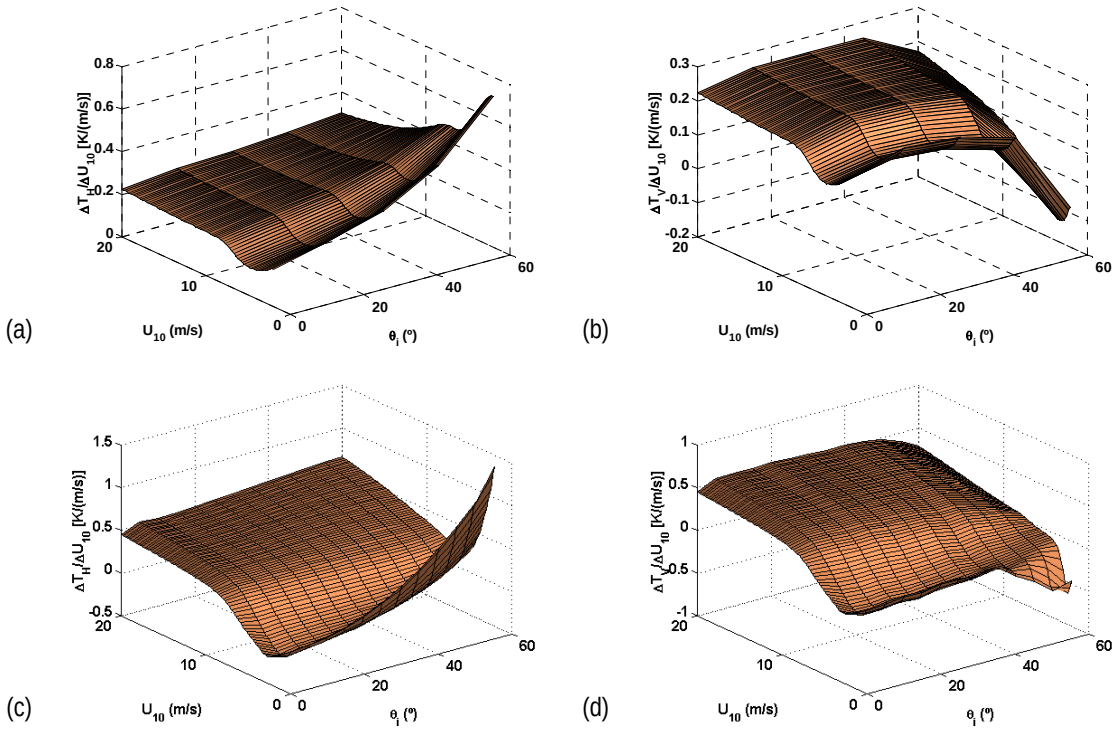

Figure 4.11. Predicted wind speed sensitivity using the SSA method and Durden and Vesecky spectrum times 2 [34] (a,b) or Elfouhaily et al. spectrum times 2 [33] (c,d) at horizontal (a,c) and vertical (b,d) polarizations.

On the other hand, the lack of accuracy of the sea spectra at low winds can be appreciated in Figure 4.11. Since 45% of the measurements were performed with wind speeds in the range 0-5 m/s, 34 % in the range 5-10 m/s and only 21% in the range > 10 m/s, it is clear that an error in the computed sensitivities at low winds has a very large impact in the weighted average.

To check this issue, Figure 4.12 shows the results of processing WISE 2001 data, but retaining only data points corresponding to wind speeds larger than 2 m/s. The resulting brightness temperature sensitivity to wind speed at H- and V- polarization can be rewritten as:

$$\Delta T_H(U_{10}) = 0.25 \cdot \left(1 + \theta/118^\circ\right) \cdot U_{10} \ , \tag{4.10}$$

$$\Delta T_V(U_{10}) = 0.25 \cdot \left(1 - \theta/45^\circ\right) \cdot U_{10} \ . \tag{4.11}$$

for $U_{10} \geq 2$ m/s.

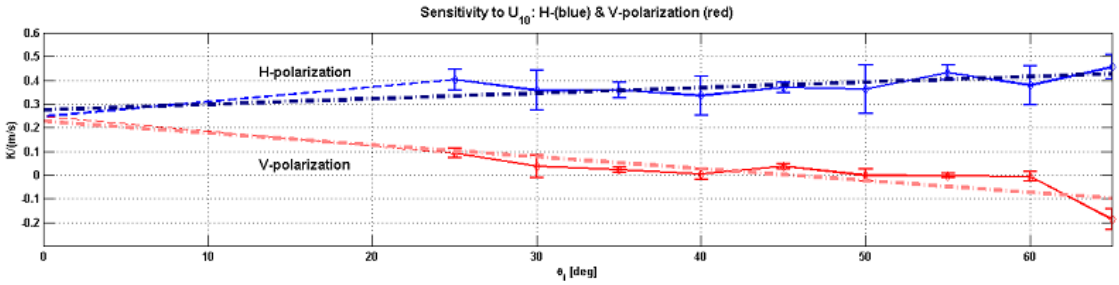

Figure 4.12. Derived wind speed sensitivity as a function of polarization and incidence angle. Only data points with U_{10} > 2 m/s have been retained.

The extrapolated sensitivity at nadir is 0.25 K/(m/s), larger than in eqn. (4.8), and the agreement improves, even at vertical polarization and mid-range incidence angles, although the model predicts a flatter behavior.

IV.3.1.3 Sea state effects on the instantaneous brightness temperature. Brightness temperature standard deviation sensitivity to wind speed

In order to investigate the modulation of the instantaneous brightness temperature by sea state, the instantaneous brightness temperature sequences have been Fourier transformed, low-pass filtered, converted from frequency to wavenumber (assuming deepwater conditions), and compared to the sea slope spectra derived from LODYC's Waverider buoy (Buoy 3), moored in front of radiometer's FOV. Since one of the parameters measured by this instrument was the height spectrum and period of the waves, the slope spectrum is computed considering that the omni-directional spectrum, the elevation $S(k)$ is proportional to the slope $P(k)$, [33] as the eqn. (4.12):

$$P(k) = k^2 \cdot S(k) \ , \tag{4.12}$$

where k is the wave number.

In Figure 4.13 the complete process is shown. The incidence angle was 45° and the radiometer position was pointed to the West. Wind direction was 10° from North and its average value was 13.6 m/s. The instantaneous brightness temperature variations are larger at vertical than at horizontal polarization (Figure 4.13a), according to the derivative of the brightness temperature with the incidence angle. In Figure 4.13b and Figure 4.13c, the instantaneous brightness temperature sequences at the two

polarizations were Fourier-transformed, and low-pass filtered. The conversion from frequency to wavenumber is shown in Figure 4.13d. Looking to the maximum peak of the instantaneous brightness temperatures spectrum it seems that the most probable wave period during the measurements was ≈10 sec. Figure 4.13e shows the height spectrum and slope variance measured by the Waverider (Buoy 3), computed according to eqn. (4.12) with the corresponding measured spectrum.

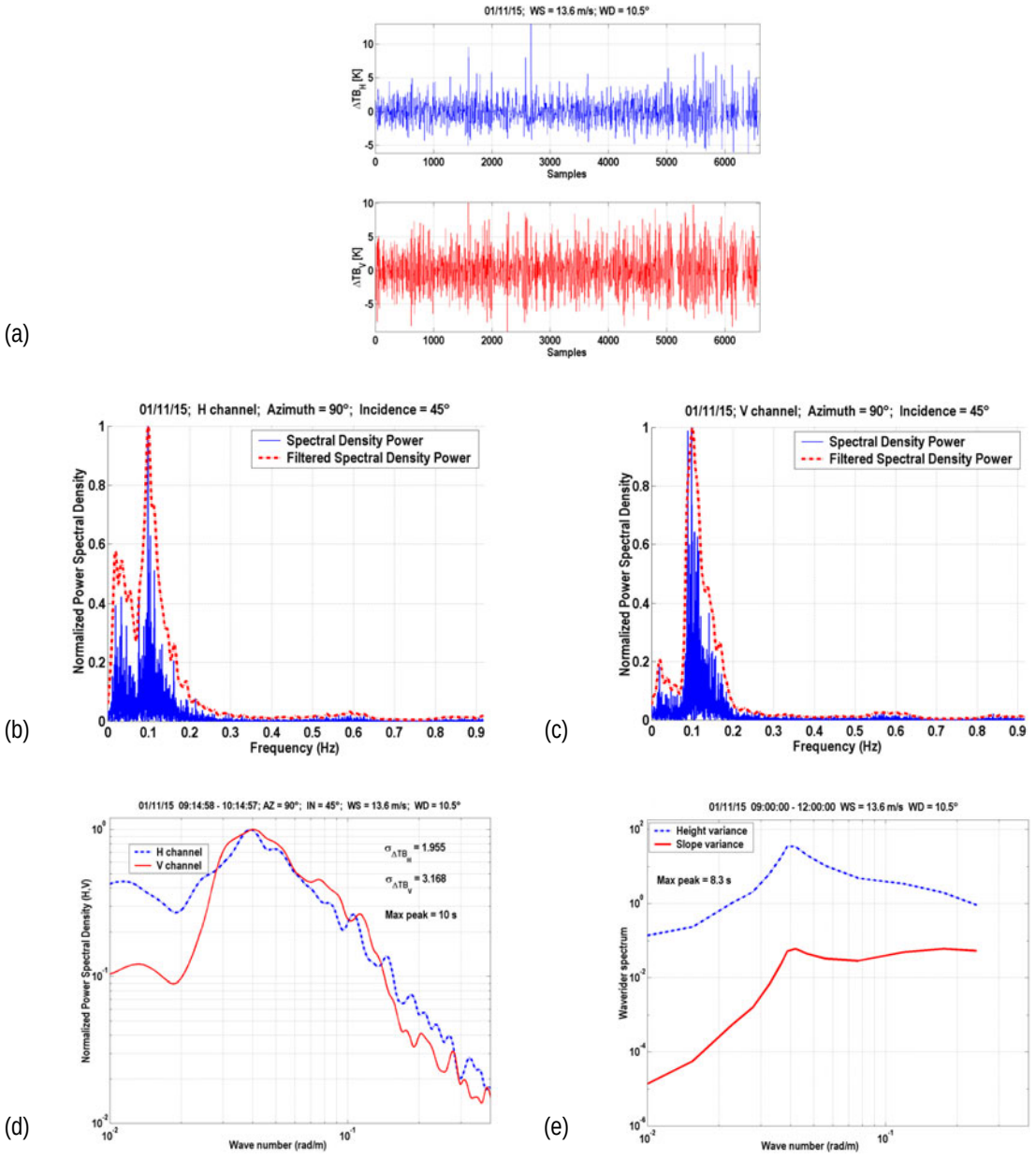

Figure 4.13. Sea state effects-induced brightness temperature (T_B). (Incidence sequence, November 15th, 2001), (a) instantaneous T_B for H- (blue) and V- (red) polarizations (1 sample = 1second). Fourier transform of the instantaneous T_B (solid blue line), filtered spectral density power (dashed red line), (b) H-, (c) V- channel, (d) instantaneous T_B normalized power spectral density (H-polarization dashed blue line, V-polarization solid red line), and (e) variance spectrum measured by the Waverider (Buoy 3), (slopes: solid red line, heights: dashed blue line).

Figure 4.13a and Figure 4.13b show two Fourier-transformed instantaneous brightness temperature sequences at H- and V- polarization, the incidence angle (θ) was 65°, the average wind direction was 11° and its mean value 11 m/s. In the first sequence the radiometer was pointing to an

azimuth ϕ = 260° North, and the second the azimuth was 320° North. The duration of each sequence was 5 minutes approximately.

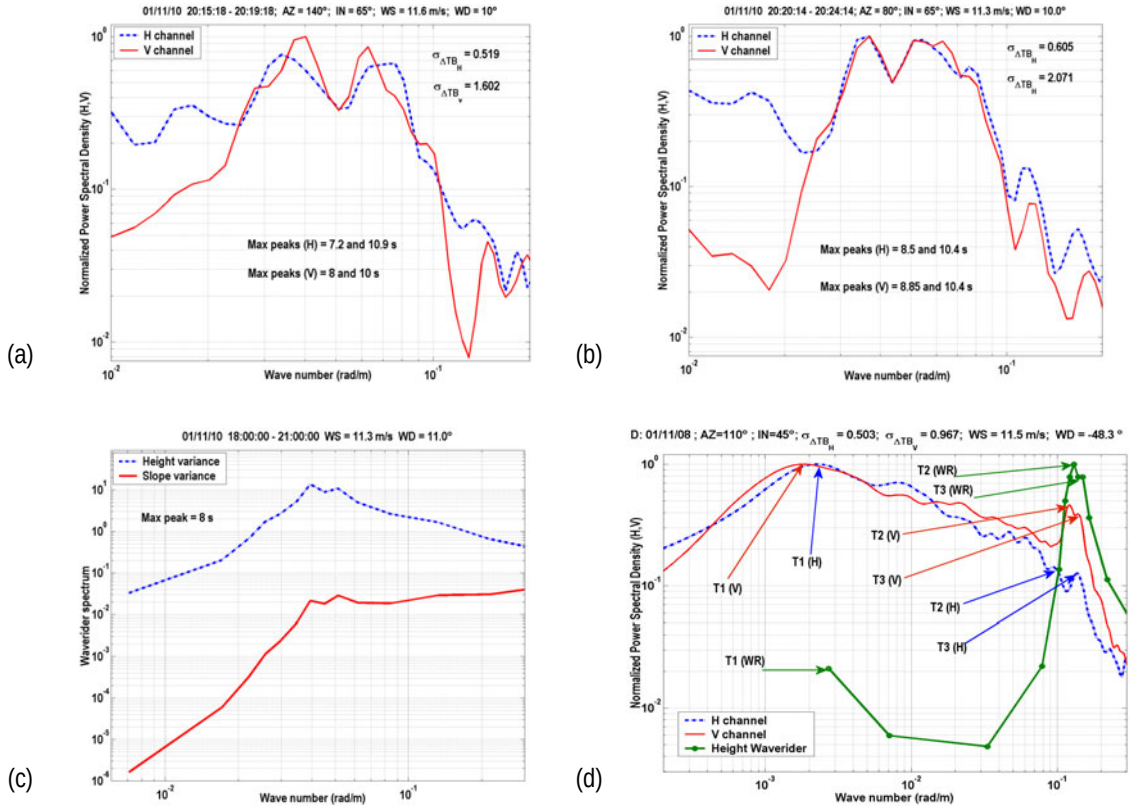

Figure 4.14. Instantaneous T_B normalized power spectral densities (NSDP), (H-polarization dashed blue line, V-polarization solid red line). Radiometer was pointed at to different azimuth angles, (a) ϕ = 260° N, (b) ϕ = 320° N, (c) variance spectrum measured by the Waverider (Buoy 3) (slopes: solid red line, heights: dashed blue line), and (d) inter-comparison of the NSDP (H-polarization dashed blue line, V-polarization solid red line) and the spectrum height variances measured from Buoy 3 (solid green line). In Table 4.3 the three most probable wave periods (T1, T2 and T3) are shown. (Large value of T1 could be due to the swell effect).

Figure 4.14c shows the height and slope variance spectrum measured by the Buoy 3, corresponding to three hours. Note the two-peak spectrum in Figure 4.14a to Figure 4.14c.

Figure 4.14d shows another measurement corresponding to an incidence scan. The radiometer was pointing to θ = 110°, WS = 11.5 m/s and WD = 312°. In this figure it can be observed the two maximum peaks of the instantaneous T_B power spectral density at both polarizations. The wave number is approximately the same of the spectral height variances. On the other hand it is appreciated the eefect of the long waves probably associated to the swell effects. Table 4.3 presents the more representative wave periods.

Table 4.3. Representative three most probable wave periods (T1, T2 and T3) from Figure 4.14 d. The large value of T1 may be due to the swell effect.

Period (s)	Horizontal polarization	Vertical polarization	Spectrum height variances
T1	42.3	46.9	38.6
T2	6.6	5.8	5.6
T3	5.4	5.2	5.4

Figure 4.15 presents the sensitivity of the standard deviation of the measured brightness temperature to wind speed at H- and V-polarizations as a function of wind speed for incidence angles from 25° to 65°.

The lower values of sensitivity at θ = 30°, 40°, 50° and 60° (measurements pointing to the North-East) are attributed to the destructive interference of the waves incident and reflected on the oil rig, a phenomenon that is also responsible of the lower sea foam coverage as a function of wind speed measured during WISE 200. The sensitivity of the brightness temperature standard deviation sensitivity to wind speed at both polarizations is approximately 0.10-0.15 K/(m/s), and it is nearly independent on incidence angle.

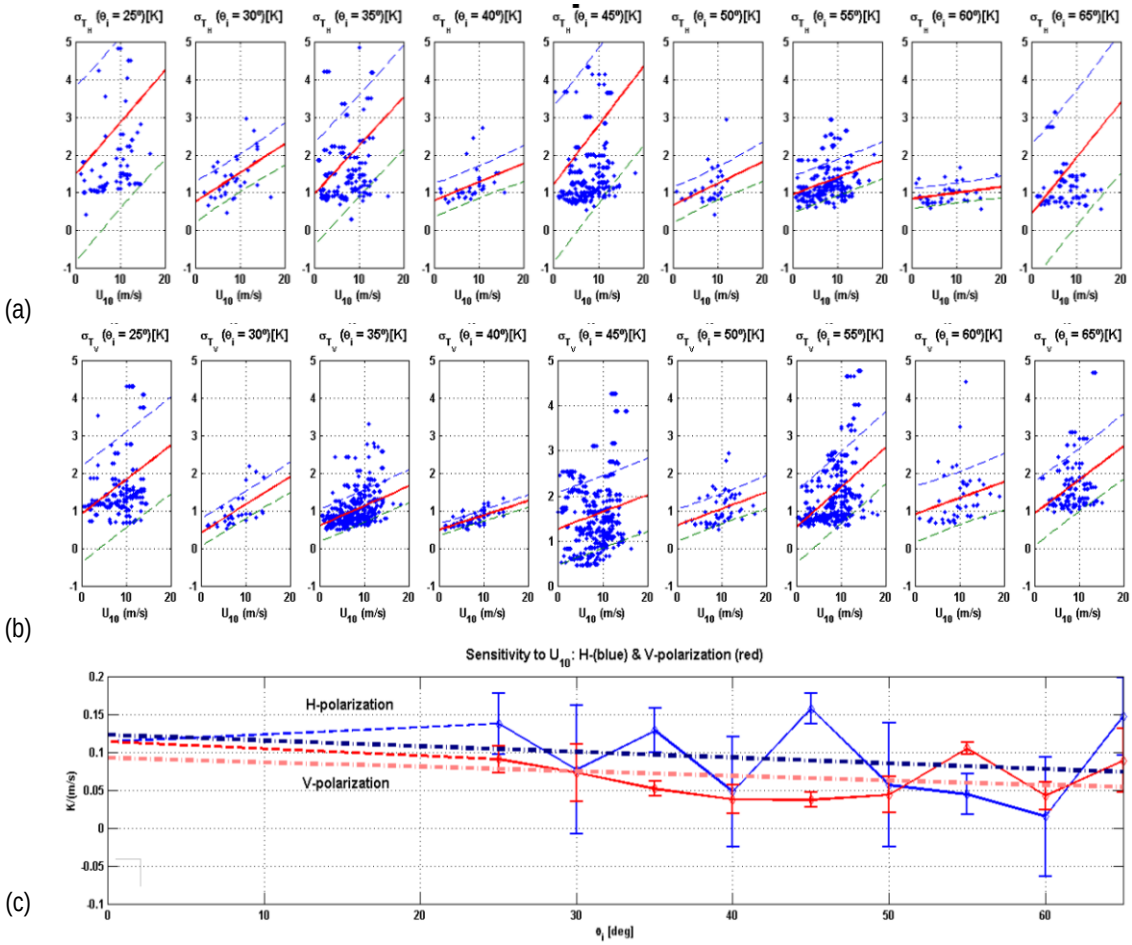

Figure 4.15. Derivation of the brightness temperature standard deviation sensitivity to wind speed: (a) H-polarization and b) V-polarization scatter plots, linear fit (solid line) and percentile 50% (dashed lines) as a function of wind speed for incidence angles from 25° to 65°. c) Derived wind speed sensitivity as a function of polarization and incidence angle. All data points used.

IV.3.2 Azimuth scan measurements

These scans were divided in order to the wind speed (U_{10}) force. During WISE 2000 and part of WISE 2001, wind conditions were low-to-moderate. Figure 4.16 shows typical measurements of azimuth scans at horizontal (left) and vertical (right) polarizations for three different wind speeds and incidence angles: (a-b) θ = 25º, U_{10} = 2.7 m/s, (c-d) θ =45º, U_{10} = 2.8 m/s, and (e-f) θ = 35º, U_{10} = 10.9 m/s. In these

plots azimuth angles are referred to the up-wind direction. It should be noted that the number of data points is very reduced, and in most scans there are missing points due to RFI, especially those pointing to the North. Even though there are very few data points covering about one third of a full 360º scan, a small 0.1-0.2 K difference is detected. Although not very accurate at L-band, an extended Kirchhoff model under the stationary phase approximation [35] was used to plot the solid lines overlaid in Figure 4.16.

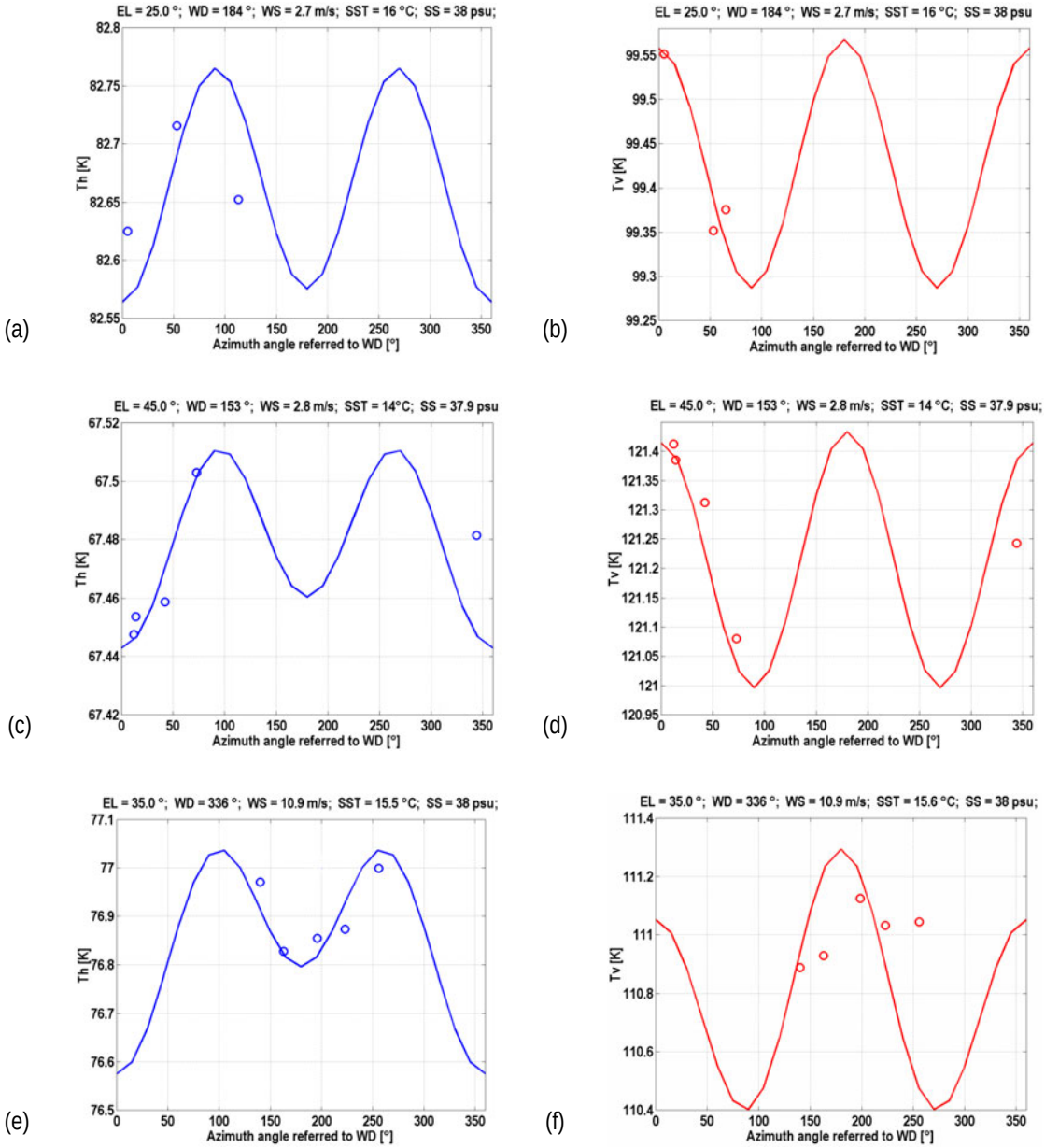

Figure 4.16. Sample measurements of azimuth scans at horizontal (left) and vertical (right) polarizations for three different wind speeds and incidence angles: (a-b) θ = 25º, U_{10} = 2.7 m/s, (c-d) θ = 45º, U_{10} = 2.8 m/s, and (e-f) θ = 35º, U_{10} = 10.9 m/s.

During November 10th and 15th, 2001, the two strongest storms were registered in the oil rig since it exists. Meteorological and oceanographic conditions were similar in both storms. Figure 4.17 shows the sea state on November 15th storm. Only measurements corresponding to November 10th are available, since the radiometer control was lost on November 15th, around 11 AM.

(a)  (b) 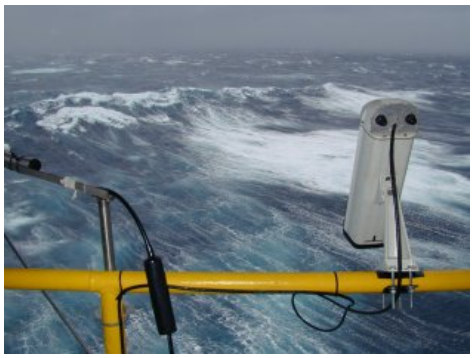

Figure 4.17. Views of the sea from the 32 m deck during the storm on November 15th, 2001: a) North-West, b) West.

Figure 4.18a and Figure 4.18b show a time series of consecutive measurements (one sample per second) at vertical and horizontal polarizations for various azimuth angles at 45° incidence angle. Average wind speed at 10 m is just 11.0 m/s, but the significant wave height corresponds to the highest peak in Figure 4.6e. The large standard deviation of the measurements –several Kelvin- is due to the brightness temperature modulation produced by the waves [36], and the highest brightness temperature peaks correspond to wave breaking events, when foam is produced. Note also the correlation between the values averaged at each azimuth angle and the azimuth angle, and that the average value is approximately the same when the radiometer points again to the same azimuth angle 20 minutes later (samples around 1000 and 2000). Figure 4.18c and Figure 4.18d show the average value (crosses) and the average value plus minus one standard deviation (triangles) of the values shown in Figure 4.18a and b. at each azimuth angle (Figure 4.18e). Figure 4.19 shows another azimuth scan at 55° incidence angle. As in the former case, the T_V and T_H signals have a standard deviation larger than instruments radiometric sensitivity, but the average values are correlated to the azimuth angle. As it can be appreciated the amplitude of the azimuth signal is smaller in T_V than in the former case, since the sensitivity to wind speed cancels around 55° incidence angle (Figure 4.12).

Table 4.4 summarizes the peak-to-peak variations at different wind speeds and incidence angles computed with the SSA method and Elfouhaily et al. sea spectrum. The measured amplitude modulations are too large as compared to model predictions (even if Elfouhaily et al. sea spectrum were multiplied by two). Further research is needed to understand its origin: the foam emission (FROG field experiment Chapters V, and VI), and the asymmetric foam distribution that is currently carried out at the UPC facilities of the Laboratorio de Ingeniería Marítima (LIM) (Figure 4.20).

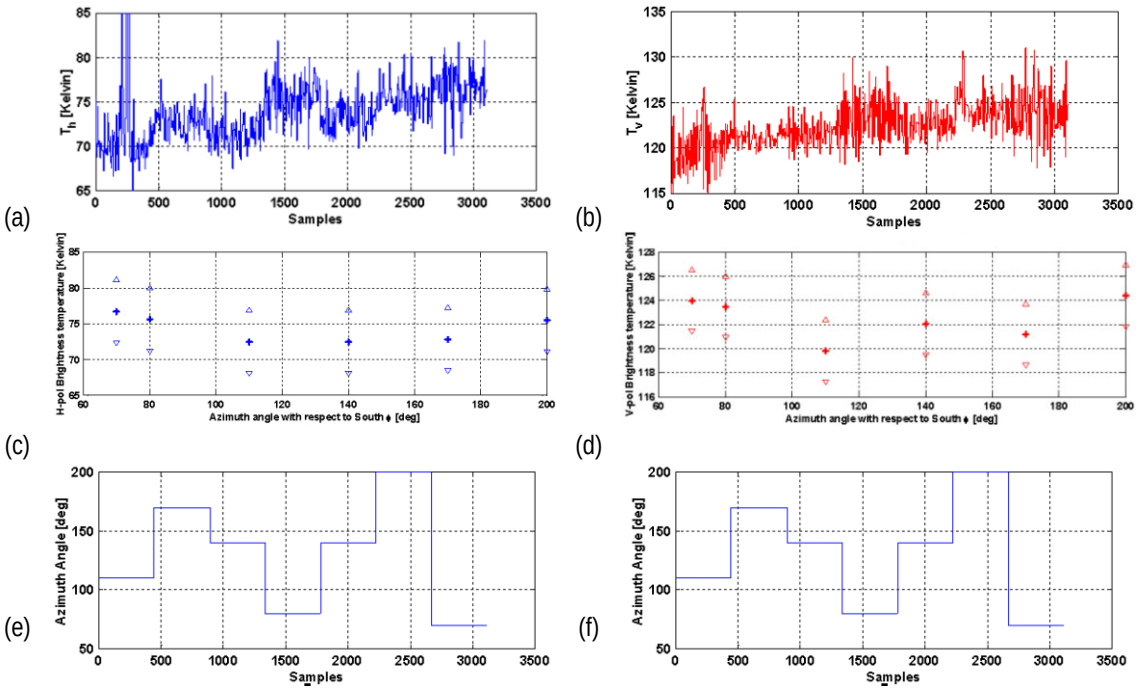

Figure 4.18. Series of samples acquired during an azimuth scan at 45° incidence angle. November 10th, 2001, 19 h. U_{10} = 11.0 m, (a) H-polarization (b) V-polarization. Average values and average values plus minus one standard deviation for each azimuth angle corresponding to (a) and (b), (c) H-polarization, and (d) V-polarization, and (e, f) azimuth angle (ϕ) with respect to the South.

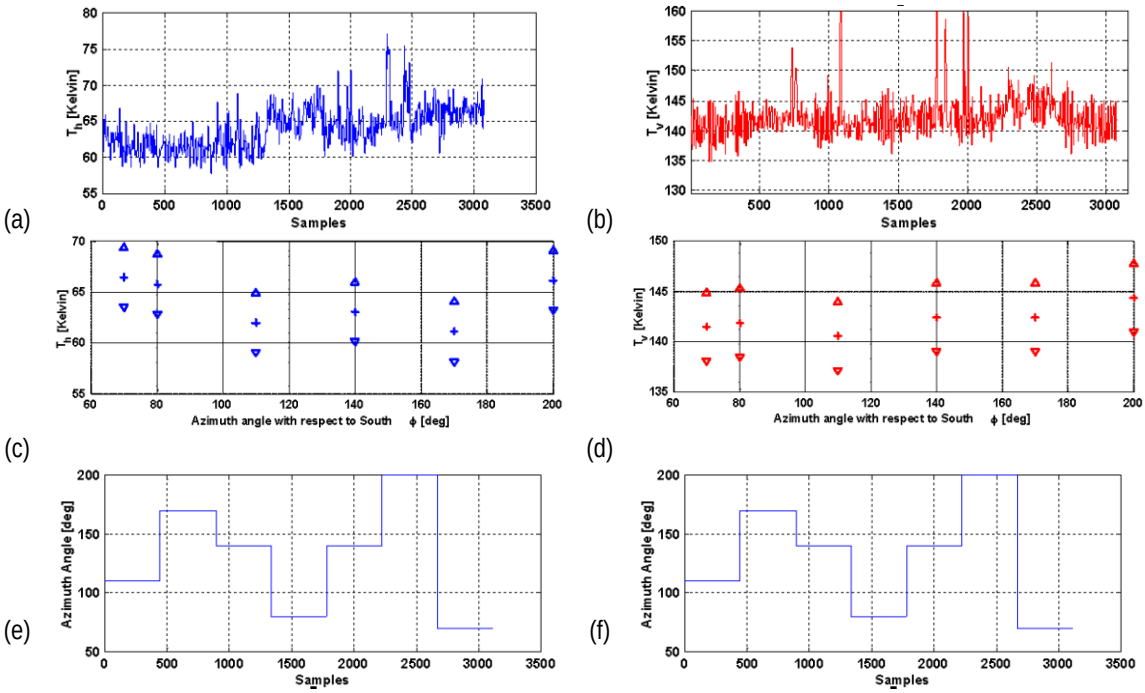

Figure 4.19. Series of samples acquired during an azimuth scan at 55° incidence angle. November 10th, 2001, 20 h. U_{10} = 12.4 m, (a) H-polarization, (b) V-polarization. Average values and average values plus minus one standard deviation for each azimuth angle corresponding to (a) and (b), (c) H-polarization, and (d) V-polarization, and (e, f) azimuth angle (ϕ) with respect to the South.

Table 4.4. Computed peak-to-peak azimuth modulation of the brightness temperature for different wind speeds using the SSA method and Elfouhaily et al. sea spectrum. Other parameters: SSS = 38 psu, SST = 20°C.

θ	0°	25°	35°	45°	55°
U_{10} = 5m/s	0.46/0.46	0.48/0.53	0.44/0.60	0.39/0.63	0.28/0.58
U_{10} = 10m/s	0.48/0.48	0.53/0.57	0.49/0.62	0.41/0.61	0.29/0.47
U_{10} = 15m/s	0.63/0.63	0.66/0.70	0.61/0.73	0.53/0.69	0.39/0.44
U_{10} = 20m/s	0.78/0.78	0.85/0.87	0.79/0.90	0.68/0.81	0.52/0.46

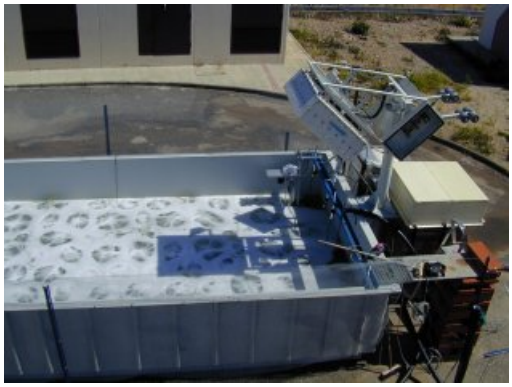

(a)

(b)

Figure 4.20. Foam experiments, (a) emissivity foam measurements (FROG) and, (b) foam distribution over the waves experiment (UPC facilities).

IV.4 WISE results: Sea foam effects on the instantaneous T_B measurements

IV.4.1 Introduction. Macroscopic and microscopic foam structure, foam formations

In the presence of foam, the sea brightness temperature (T_B) at H- and V-polarizations measured can be written as:

$$T_{B_{H,V}}^{Total}(\theta) = F(U_{10}) \cdot T_{B_{H,V}}^{Foam} + [1 - F(U_{10})] \cdot T_{B_{H,V}}^{Sea} \tag{4.13}$$

where $F(U_{10})$ is the fractional sea foam coverage that, among other factors, mainly depends on the 10 m wind speed (U_{10}), θ is the incidence angle, and $T_{B_{H,V}}^{Foam}$ and $T_{B_{H,V}}^{Sea}$ are the brightness temperatures of 100 % foam-covered and foam-free, respectively [37].

Basically, foam is composed by a mixture of air bubbles and water generated by the breaking of the sea. The brightness temperature increase not only depends on the fractional area collected at any instant by the radiometer. Moreover, it is necessary to take into account the volumetric distribution and the foam formations [25]. Attending to the foam formations, these can be classified into two groups (Figure 4.21): a thick one formed by whitecaps, and a thin one called foam streaks. Whitecaps are very poor reflectors of radiation [38], and consequently its emissivity is large. Streaks are generated mainly by Langmuir circulation, but the emissivity it is not so high because of the poor volumetric foam content. This classification in two groups was made by Monahan [39] who introduced two terms: “Stage A” referred to

the strong breaking waves, and "Stage B" referred to the old foam and foam streaks. Additionally it is interesting to classify the foam formations attending to their lifetime or stability. Whitecaps' lifetime is very short, only a few seconds, since they are unstable. On the other hand, streak and thin foam generated by Langmuir circulation are stable with a lifetime of several minutes, and sometimes even hours.

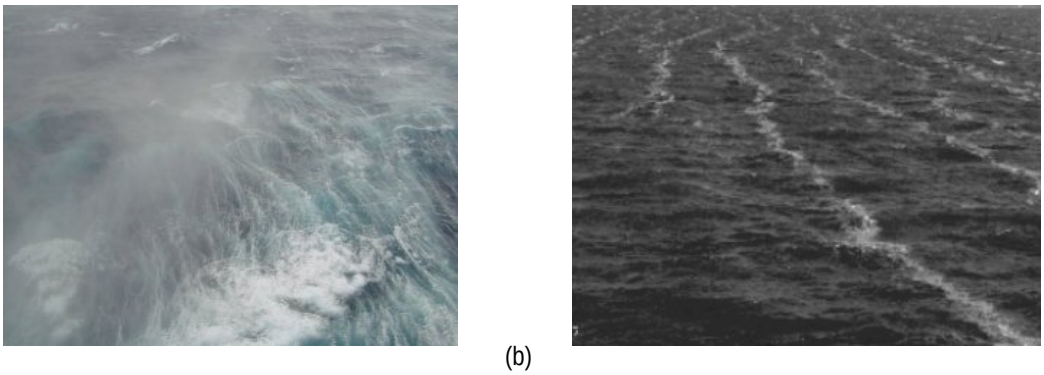

(a) (b)

Figure 4.21. Examples of foam formations, (a) Whitecaps, and (b) foam streaks (South Hampton, Alex Smith).

Another interesting parameter is the relationship between the foam persistence time (τ_{foam}) and the wave period of the breaking wave (T_{break}). Figure 4.22 shows a model of the foam-layer persistence time [25], and the bubbles structure associated with the breaking waves [40] and [41]. Three phases, at least, of the foam development should be considered:

- The α-plume is the subsurface extension of the turbulent bore of a spilling breaker, or the entraining jet of a plunging breaker, or both. The α-plume contains all the active entrainment and it belongs to the "Stage A",
- The β-plume is the remnants of an α-plume once the turbulence of the entrainment flow has sub-sided that belongs to the beginning of the "Stage B", and
- The γ-plume, that consists of the mature β-plume.

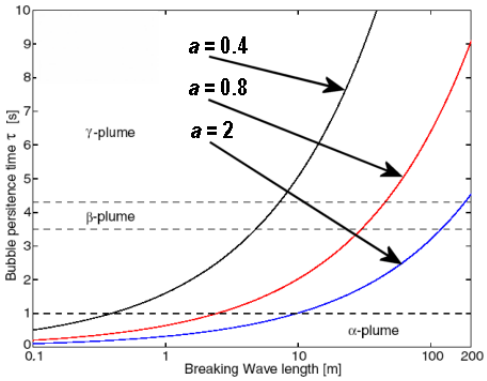

Figure 4.22. Values of the bubble persistence average time (τ_{foam}) as function of breaker wavelength (T_{break}) for three values of the parameter: a = 0.4, a = 0.8 and a = 2 [25].

According to this model, the quotient ($a = \tau_{foam}/T_{break}$) is an indicator parameter of the foam type: static or dynamic. For large a, the foam persistence is high with respect the wave period of the breaking

wave, and probably fossil foam can be considered. On the contrary, if *a* is small active foam is produced. Figure 4.22 reflects three different values of *a* = 0.4, 0.8 and 2.

In general the foam is modeled by a structure with several layers. Air bubbles and water shells are geometrically organized within the layer. According to [42] the foam is classified by the inner structures into four groups:

- Mono or poly-dispersed system of spherical particles,
- Continuous structure of close-packed spherical bubbles,
- Cellular system close-packed bubbles with irregular polyhedral shapes (Figure 4.23a),
- Dry foams formed by thin liquid films.

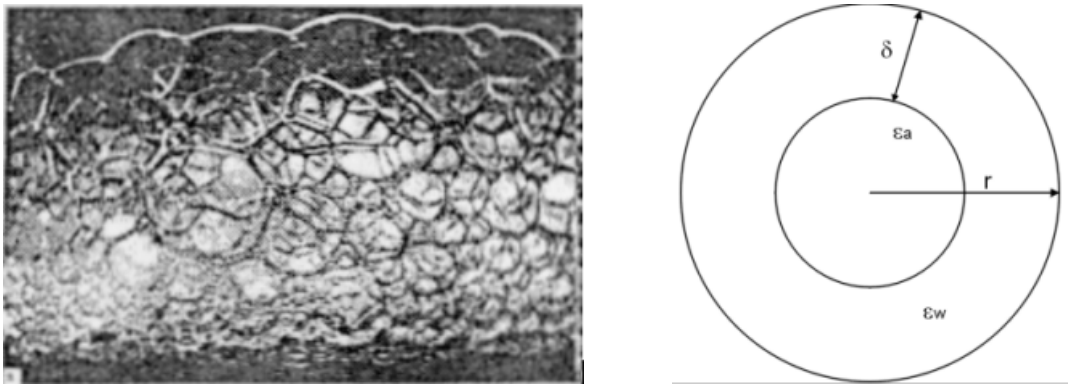

(a) (b)

Figure 4.23. (a) Picture of a cross-section through a multi-layer honeycomb foam structure generated in the laboratory [43], and (b) spherical water coated bubble: r is the outer radius, δ is the water-coating thickness, and ε_a and ε_w are the dielectric permittivity of air and water respectively.

Attending to [25] the first group classification, the shape of the bubbles can be approximated by spheres with different radius that in general increase with age. The spherical approximation simplifies the computation of the electromagnetic problem. Figure 4.23b shows an schematic representation of the bubbles formed by an air core surrounded by a water shell.

IV.4.2 Sea foam coverage as a function of the wind speed

Another important factor to compute the total emissivity is the stickiness parameter also (called packing coefficient). The packing coefficient is inversely proportional to the strength of the attractive force between bubbles. Other factors are: the foam layer thickness, the air bubbles bellow the foam layers, the physical temperature of sea surface, etc that are required in the electromagnetic models. Numerical simulations will be compared to WISE radiometric data.

The relationship between foam coverage and wind speed of the measured data from WISE 2000 is presented in Figure 4.24 a. Data points were derived by linear regressions of the log-log plots that are:

$$F(U_{10}) = 2.32 \cdot 10^{-6} \cdot U_{10}^{3.4988}. \qquad (4.14)$$

Typical foam coverage variations between 2% and 3% at a U_{10} = 15 m/s were obtained from the WISE 2000 data, by observing its linear regression. On the other hand, it is clear that foam coverage did not only depend on the wind. The high dispersion of some data points was probably due to the following effects:

- The sea state,
- The fetch: the wind direction determined clearly the size of the waves. Mainly, the waves generated when the wind blew from the NW (40 Km offshore) were smaller than the waves formed when the wind direction blew from the East and NE (longer fetch), and
- The oil rig structure produced interference on the waves formations.

During WISE 2000 the sea-air temperature difference ΔT was moderated and the atmosphere was almost neutral all the time, and hence no wind speed correction was necessary to be applied. The inter-comparison of the empirical WISE 2000 regression and the Monahan and O' Muircheartaigh, the Bordum and Sharkov, and Monahan and Woolf semi-empirical models [25], seems to conclude that the presence of static foam was the most important during WISE 2000 Figure 4.24b.

(a)

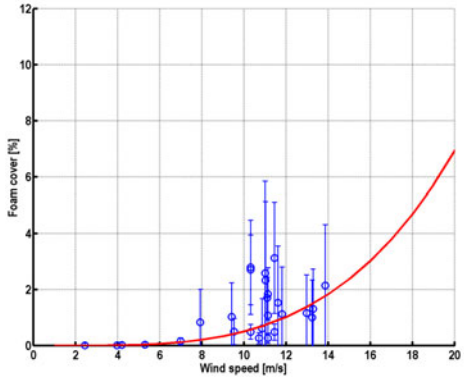

(b)

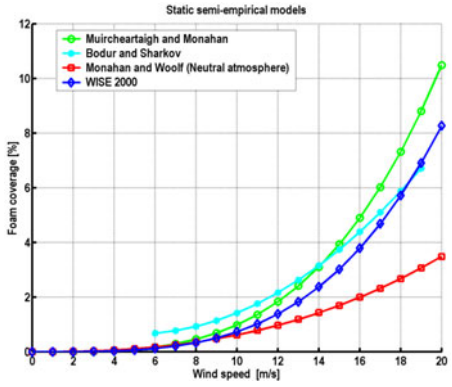

Figure 4.24. Foam coverage as a function of the wind speed, (a) WISE 2000's data samples, and (b) static semi-empirical models.

However during WISE 2001 the sea-air temperature difference was above 2°C all the time, and reached 12°C. The atmosphere was very unstable. Since wind speed measurements needed to be referred to 10 m height, atmospheric stability effects have to be taken into account [26]. If they were not, the wind speed dependence would exhibit a lower power:

$$F(U_{10}) = 3.49 \cdot 10^{-6} \cdot U_{10}^{2.9235} \ , \tag{4.15}$$

but when applying the wind speed correction [26],

$$F(U_{10}) = 0.43 \cdot 10^{-6} \cdot U_{10}^{3.6824} \tag{4.16}$$

The power coefficient is much closer to the stable case (eqn. (4.16))

Additionally it is important to consider the temperature difference between the air and the water $\Delta T = T_{sea\_water} - T_{air}$ [38]. If the water is warmer than the air, more foam formations are generated. For example if ΔT = 10 °C the increase of $F(U_{10})$ is a factor of 2.4 [44].

In Figure 4.25 all the foam coverage data points are represented as a function of the wind speed and fitted by a curve (eqn.(4.15)). Depending on ΔT the WISE 2001, $F(U_{10})$ will be different as it can be shown in ellipses marked on the Figure 4.25. In general for ΔT between -2 °C and -6 °C, most foam coverage was generated for the same wind speed conditions than for other ΔT values.

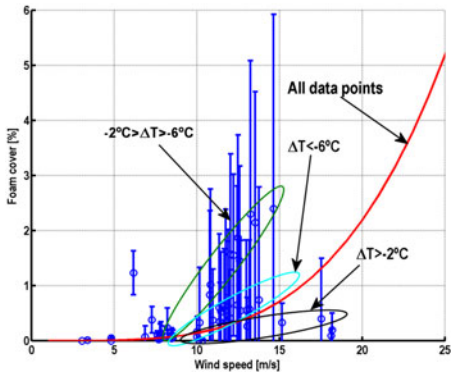

Figure 4.25. WISE 2001's foam coverage as a function of the wind speed (all data samples).

By observing the data points were classified inside of three ellipses:

- Most of the data points are included between the range of -2°C>ΔT>-6°C (green ellipse) In this case the atmosphere starts to be unstable and static foam is predominant over dynamic one.
- Data points inside of the cyan ellipse correspond to a ΔT<-6°C (very unstable conditions). In theses cases, dynamic foam was considered ("STAGE A", essentially α-plume was generated) and, hence the foam persistence time is less than for fossil foam Figure 4.22.
- The points inside of the black ellipse correspond to a ΔT>-2°C (neutral conditions of the atmosphere).

IV.4.3 Experimentally-derived sea foam brightness temperature

Unfortunately during WISE 2000, most of the data points were collected for wind speeds lower than 10 m/s. The highest wind speed registered was 18 m/s. However, during WISE 2001 the meteorological conditions were the most extreme ones registered on the oil rig during the past 20 years. During more than one third of the campaign, winds well exceed 10 m/s, exceeding 25 m/s, when the strongest storm happened.

From the inspection of the ~ 63,000 photograms analyzed in WISE 2001, the first conclusion is that for wind speeds smaller than 8-9 m/s, the foam coverage is negligible, and hence there is no associated

brightness temperature increase. During November 8th to 17th, 2001, there is a complete set of imagery data corresponding to an average wind speed of 13 m/s that have been used to estimate the sea from emissivity. To process these sequences, the starting point consisted of representing the variation of brightness temperature ΔT_B with respect to the mean value in that period versus the instantaneous foam coverage. Figure 4.26a and b show samples of the corresponding scatter plots at H and V-polarizations. The large scatter at low foam coverage is due to the radiometer's noise, and the brightness temperature modulations due to waves' slopes, as it will be shown in the next sections. Outlier data points are iteratively eliminated when they deviate more than 3σ from the linear regression. The process converges quickly as shown in the iterations in Figure 4.26. The slope of the linear fit is equal to the $T_{B_{h,v}}^{Foam}$ in (4.13).

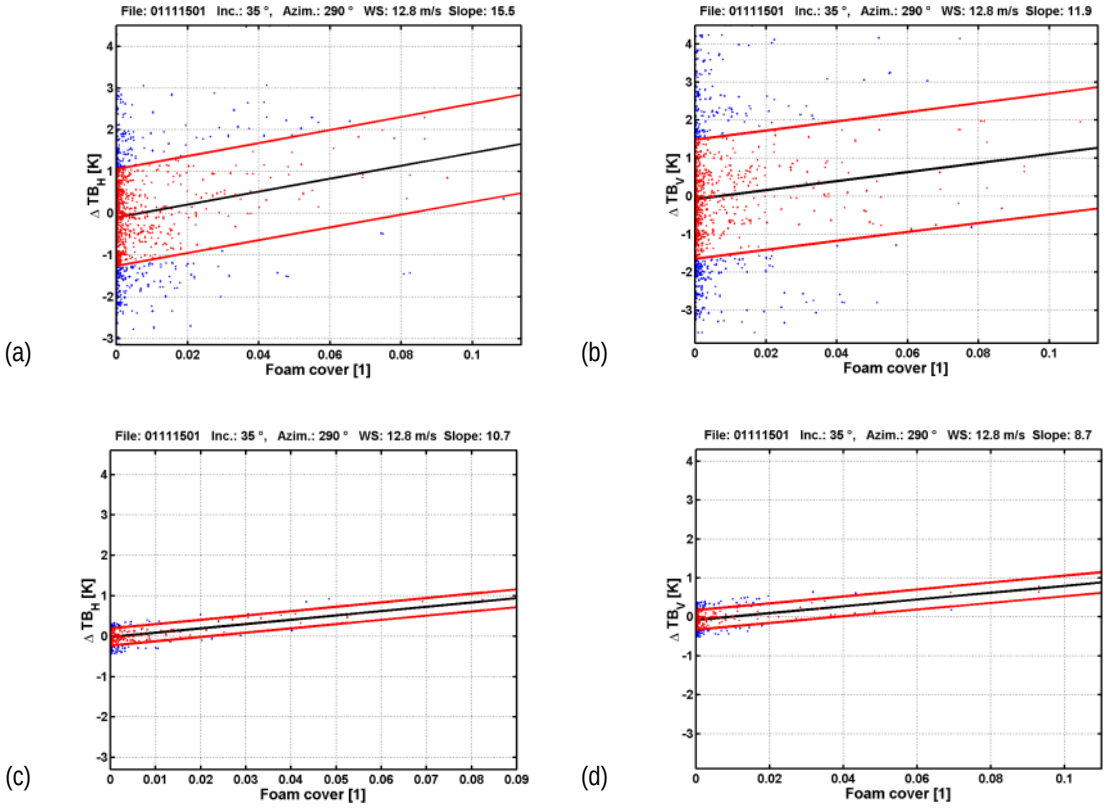

Figure 4.26. Iteration process to get a relation between ΔT_B and foam coverage following a straight line fitted (solid line). 50% confidence levels (dotted line). 1st iteration for (a) H-channel, (b) V-channel, 4th iteration for (c) H-channel, (d) V-channel.

A classification of the processed sequences according to the incidence angle is shown in Figure 4.27. A linear regression is made at each polarization forcing that $\Delta T_H = \Delta T_V$ at nadir. The foam brightness temperature increases from 10 K to 15 K, from θ = 25° to 65° at the vertical polarization, and there is almost no dependence for the horizontal polarization.

According to eqn. (4.13) the brightness temperature increase can now be computed as:

$$\Delta T_B = T_{B_{H,V}}^{Total} - T_{B_{H,V}}^{Sea} = F(U_{10}) \cdot \left(T_{B_{H,V}}^{Foam} - T_{B_{H,V}}^{Sea} \right) = F(U_{10}) \cdot \Delta T_B \qquad (4.17)$$

with, for example, the WISE-derived $F(U_{10})$ (Figure 4.25a) and $T_{B_{H,V}}^{Foam}$ (4.17).

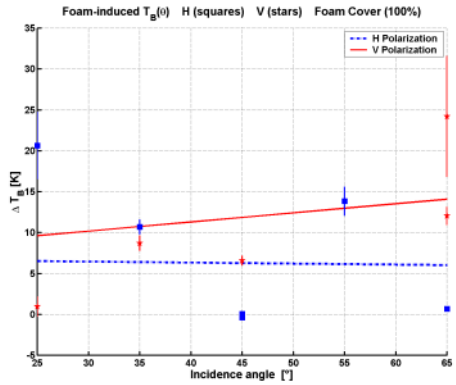

Figure 4.27. Brightness temperature induced as a function of the incidence angle for a complete foam-covered spot radiometer. (F=100%).

Due to the large scatter in $F(U_{10})$, the foam induced ΔT_B is defined by a central value and an upper and lower limits. For example the foam-induced brightness temperature is:

- 0.06 K ($\pm$ 0.03 K) at H- and V- polarizations at 15 m/s and θ= 0°,
- 0.1 K (+ 0.03 K, -0.06 K) at V-polarization and 0.06 K (+0.03 K, -0.04 K) at H-polarization at 15 m/s and θ= 30° (Figure 4.28a), and
- 0.11 K (+0.06 K, -0.07 K) at V-polarization and 0.06 K (+0.03 K, -0.04 K) at H-polarization at 15 m/s and θ= 50° (Figure 4.28b).

In order to reduce the errors associated to the estimation of T_B (Figure 4.27) a different controlled experiment had to be performed (Chapter VI).

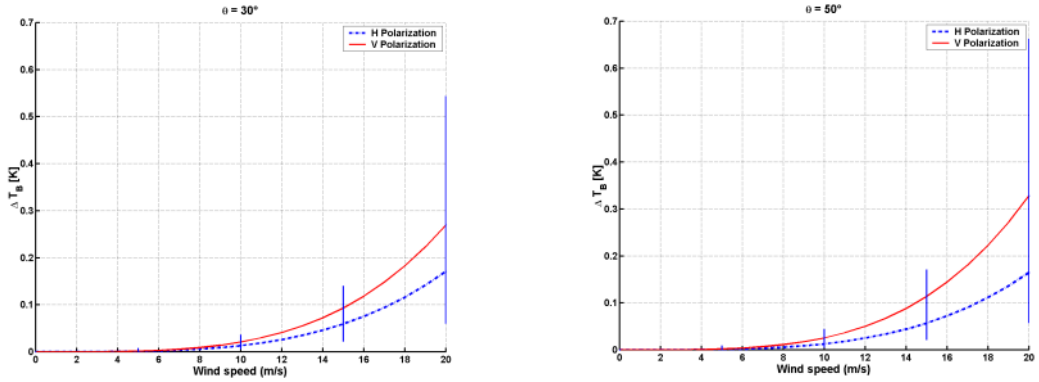

(a) (b)

Figure 4.28. Brightness temperature induced as a function of WISE 2001, $F(U_{10})$, (a) θ= 30°, and (b) θ= 50°.

It is worth noting that foam-induced brightness at vertical polarization is higher that at horizontal polarization, which is the opposite than at higher frequencies [45].

IV.4.4 Inter-comparison with the two-layer theoretical model

Applying the two-layer model [25] to compute the foam-induced ΔT_B, but taking into account WISE 2001 $F(U_{10})$, with a gamma distribution of bubble radius, a typical average radius of r_p = 250 μm, a stickiness factor of κ = 0.1, a foam thickness of d = 2 cm, a bubble's water coating thickness of δ = 20 μm and assuming that the air fraction beneath the foam layer is f_a = 0.2, the foam-induced $\Delta T_{B_{h,v}}^{Foam}$ as a function of the wind speed and the incidence angle is represented in Figure 4.29. The model also seems to guess the opposite relationship between T_B and the incidence angle at H- and V-polarizations with respect to the 10.8 and 36.5 GHz. It can be seen that the foam-induced brightness temperature increase taking into account [25] the WISE 2001 sea foam coverage is actually small. The predicted ΔT_B at vertical polarization were: 0.09, 0.1 and 0.13 K at 0°, 30° and 50° incidence's angle and 15 m/s wind speed. At the horizontal polarization the values are: 0.09, 0.087 and 0.075 K for the same angles and wind speed. WISE-derived ΔT_B values are: 0.06, 0.09 and 0.11 K for 0°, 30° and 50° at vertical polarization and: 0.06, 0.06 and 0.05 K for 0°, 30° and 50° at horizontal polarization.

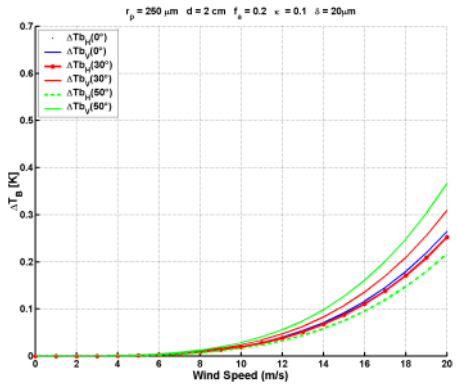

Figure 4.29. Brightness temperature induced by foam at 1.4 GHz as function of wind speed for three incidence angles: 0°, 30° and 50° solid curve: V- polarization, dashed curve: H- polarization.

IV.4.5 Other whitecap phenomenology

Foam appears suddenly when a wave breaks. Foam coverage peaks and standard deviation were also computed for all the foam sequences processed at all wind speeds. The lowest foam levels (< 5% with respect to the maxim peak) have been neglected (Figure 4.30a). The results for 21 samples (1 sample per day) are represented in Figure 4.30b. The probability density function (pdf) of a breaking event is close to an exponential (mean and standard deviation are almost equal).

Once the wave breaks, the foam patch lasts until it disappears over the sea. The lifetime constant of unstable foam was computed looking to the instantaneous foam coverage at the starting photogram when the whitecap is formed until it is extinguished. To compute this constant it is necessary to use a moving window to isolate the whitecap, (Figure 4.31). To compute the extinction time constant a sequence slides were selected. A previous condition to select the photogram was the capability to follow the foam in the work sequence. The total set of photograms analyzed was 8, and an exponential fit was applied to the result, (Figure 4.32). The average time constant was 3.15 ± 0.7 seconds. Other studies related performed

by Monahan and Lu [39], show time constant values in the range (3.5 – 4.3 s), a little bit higher than in WISE case. This may be probably due to the surface temperature, since the water kinematical viscosity (proportional to the viscous dissipation ratio) is proportional inversely to the surface temperature [46].

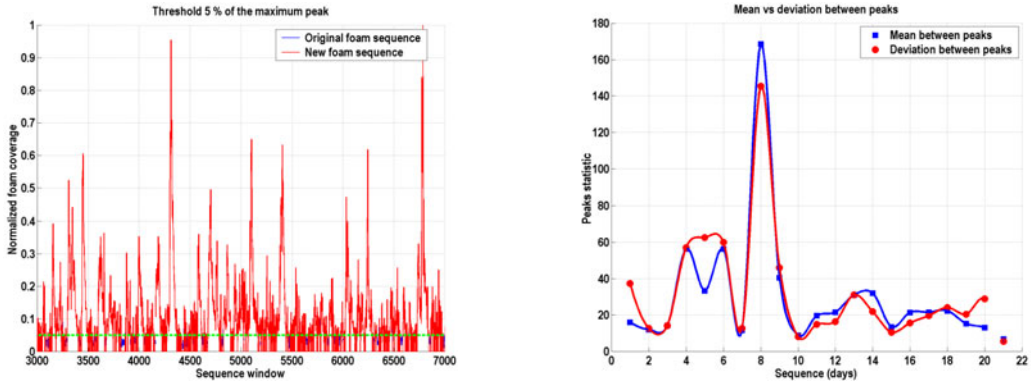

(a) (b)

Figure 4.30. (a) Removed of foam samples less than 5% of the maximum peak, and (b) mean time between foam generation peaks and standard deviation.

Figure 4.31. Typical patch of foam disappearing over the sea.

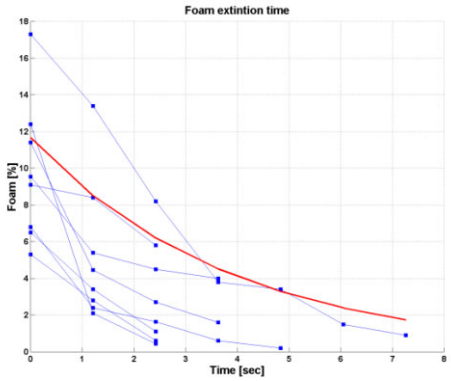

Figure 4.32. Foam extinction corresponding to eight sequences

IV.5 Conclusions

In this chapter the results from WISE 2000 and 2001 are presented. First of all and accurate explanation of the data pre-processing and processing is made. Second, the main results of the two experiments, derived from a set of radiometric and ground-truth data are compiled. The sensitivity of the brightness temperature to the wind speed is derived from the data and compared with previous measurements [28] and the models. However during WISE 2000, the error bounds were large because an important number of data samples were corrupted, probably due to the RFI. Data acquired during WISE 2001 field experiment suffered an improvement basically due to: some previous considerations from the first experiment the fact, that there were not drilling activities during this period, and fortunately different sea surface conditions were happened.

The main results derived from WISE field campaigns are summarized:

- A sensitivity to wind speed extrapolated at nadir of ~0.23 K/(m/s), or ~0.25 K/(m/s) when the atmospheric instability, or only the measurements corresponding to U_{10} > 2 m/s are accounted for.
  - An increase at *H*-polarization up to ~0.5 K/(m/s) at 65°.
  - A decrease at *V*-polarization down to ~-0.2 K/(m/s) at 65°, with a zero-crossing around 55°-60°.
  - These results are in agreement with the SSA method using Durden and Vesecky and Elfouhaily et al. sea spectra times 2. It is very likely that the computed wind speed sensitivities below 2 m/s are erroneous.
- A modulation of the instantaneous brightness temperatures due to *wave slopes* and *foam*. The standard deviation of this modulation increases with wind speed at a rate of ~0.1-0.15 K/(m/s), depending on polarization, and very weakly on incidence angle.
- A small azimuth modulation ~0.2-0.3 K for low-to-moderate wind speeds, in reasonable agreement with numerical models. On November 10th, 2001, peak-to-peak modulations of 4-5 Kelvin where measured, and explanation has been found for it (foam and wave asymetry).
- Impact of the presence of sea foam in L-band brightness temperature is estimated to be ~0.25 K at wind speeds of 20 m/s at nadir. However for the same conditions, the sea foam coverage exhibits a high variability. Hence, dedicated campaigns (FROG field experiment, Chapter VI) to determine the emissivity due to foam are necessary.
- Rain effects on the sea emission were not studied because they were very rare events, and appeared in conjunction of storms, and agitated sea. Dedicated campaigns (FROG field experiment, Chapter V, and VI) were also required.